The Plant Cell, Vol. 30: 1040–1061, May 2018, www.plantcell.org © 2018 ASPB.



# Vacuolar H$^+$-Pyrophosphatase and Cytosolic Soluble Pyrophosphatases Cooperatively Regulate Pyrophosphate Levels in *Arabidopsis thaliana*

**Shoji Segami,[a] Takaaki Tomoyama,[a] Shingo Sakamoto,[b] Shizuka Gunji,[c] Mayu Fukuda,[a] Satoru Kinoshita,[a] Nobutaka Mitsuda,[b] Ali Ferjani,[c] and Masayoshi Maeshima[a,1]**

[a] Laboratory of Cell Dynamics, Graduate School of Bioagricultural Sciences, Nagoya University, Nagoya, Aichi 464-8601, Japan
[b] Plant Gene Regulation Research Group, Bioproduction Research Institute, National Institute of Advanced Industrial Science and Technology (AIST), Higashi 1-1-1, Tsukuba, Ibaraki 305-8566, Japan
[c] Department of Biology, Tokyo Gakugei University, Koganei-shi, Tokyo 184-8501, Japan

ORCID IDs: 0000-0003-4687-5630 (S.K.); 0000-0003-1157-3261 (A.F.); 0000-0002-1611-5481 (M.M.)

**Inorganic pyrophosphate (PPi) is a phosphate donor and energy source. Many metabolic reactions that generate PPi are suppressed by high levels of PPi. Here, we investigated how proper levels of cytosolic PPi are maintained, focusing on soluble pyrophosphatases (AtPPa1 to AtPPa5; hereafter PPa1 to PPa5) and vacuolar H$^+$-pyrophosphatase (H$^+$-PPase, AtVHP1/FUGU5) in *Arabidopsis thaliana*. In planta, five PPa isozymes tagged with GFP were detected in the cytosol and nuclei. Immunochemical analyses revealed a high abundance of PPa1 and the absence of PPa3 in vegetative tissue. In addition, the heterologous expression of each PPa restored growth in a soluble PPase-defective yeast strain. Although the quadruple knockout mutant plant *ppa1 ppa2 ppa4 ppa5* showed no obvious phenotypes, H$^+$-PPase and PPa1 double mutants (*fugu5 ppa1*) exhibited significant phenotypes, including dwarfism, high PPi concentrations, ectopic starch accumulation, decreased cellulose and callose levels, and structural cell wall defects. Altered cell arrangements and weakened cell walls in the root tip were particularly evident in *fugu5 ppa1* and were more severe than in *fugu5*. Our results indicate that H$^+$-PPase is essential for maintaining adequate PPi levels and that the cytosolic PPa isozymes, particularly PPa1, prevent increases in PPi concentrations to toxic levels. We discuss *fugu5 ppa1* phenotypes in relation to metabolic reactions and PPi homeostasis.**

## INTRODUCTION

Inorganic pyrophosphate (PPi) is a high-energy phosphate compound that is generated as a by-product of over 200 metabolic reactions, including fatty acid β-oxidation and DNA, RNA, aminoacyl-tRNA, and polysaccharide biosynthesis (Heinonen, 2001; Ferjani et al., 2014). In most organisms other than plants, PPi hydrolysis is catalyzed by the soluble form of inorganic pyrophosphatase (sPPase; EC 3.6.1.1). Genetic defects in sPPase lead to the intracellular accumulation of PPi, resulting in severe growth defects or cell death owing to thermodynamic inhibition of the abovementioned essential reactions (Chen et al., 1990; Serrano-Bueno et al., 2013). In addition to orthologs of sPPase, plants also contain vacuolar H$^+$-pumping inorganic pyrophosphatase (H$^+$-PPase). *Arabidopsis thaliana* contains six paralogs of sPPase, PPa1 to PPa6 (Schulze et al., 2004; Navarro-De la Sancha et al., 2007). sPPase isozymes are classified into two families: $Mg^{2+}$-dependent enzymes in Family I and $Mn^{2+}$-dependent enzymes in Family II. The six sPPase isozymes in Arabidopsis require $Mg^{2+}$ for their activity and thus belong to Family I. Family II sPPases are found in only a limited number of bacteria and archaea (Shintani et al., 1998; Young et al., 1998).

Family I members are separated into two clades: prokaryotic and eukaryotic types (Schulze et al., 2004; Gómez-García et al., 2006). The prokaryotic type is represented by the hexameric enzyme ppa in *Escherichia coli* and the eukaryotic type by the dimeric enzyme IPP1 (INORGANIC PYROPHOSPHATASE1) in yeast (*Saccharomyces cerevisiae*). Arabidopsis sPPases PPa1 to PPa5 are of the prokaryotic type and are localized to the cytosol (Koroleva et al., 2005; Öztürk et al., 2014; Gutiérrez-Luna et al., 2016). PPa6, on the other hand, is of the eukaryotic type and is localized to plastids in Arabidopsis (Schulze et al., 2004). The subcellular localization of plant sPPases has been examined using several methods: immunogold labeling for potato (*Solanum tuberosum*) enzymes (Rojas-Beltrán et al., 1999), analysis of GFP fusion proteins for Arabidopsis enzymes (Koroleva et al., 2005; Öztürk et al., 2014; Gutiérrez-Luna et al., 2016), and an in vitro import assay for pea (*Pisum sativum*) PPa6 (to chloroplasts; Schulze et al., 2004). PPi hydrolysis activity has been detected for several sPPase isozymes in plants (Schulze et al., 2004; Gómez-García et al., 2006; Navarro-De la Sancha et al., 2007). Nonetheless, the physiological roles of these cytosolic sPPases are not fully understood.

In evaluating the physiological functions of sPPases, two points are worth considering: (1) the enzymatic activity of plant sPPases is very low and (2) cytosolic PPi concentrations are relatively high (0.2–0.3 mM) (Weiner et al., 1987). The enzymatic activity of plastid sPPases is markedly higher than that of the cytosolic isozymes, and PPi levels are lower in plastids than in the cytosol (Weiner et al.,

[1] Address correspondence to maeshima@agr.nagoya-u.ac.jp.
The authors responsible for distribution of materials integral to the findings presented in this article in accordance with the policy described in the Instructions for Authors (www.plantcell.org) are: Shoji Segami (segami@agr.nagoya-u.ac.jp) and Masayoshi Maeshima (maeshima@agr.nagoya-u.ac.jp).
www.plantcell.org/cgi/doi/10.1105/tpc.17.00911

## IN A NUTSHELL

**Background:** Many biological reactions, including the biosynthesis of DNA, RNA, proteins, and polysaccharides, produce inorganic pyrophosphate (PPi). However, accumulation of PPi at high levels suppresses cell activities, such as the biosynthesis of these macromolecules. Therefore, hydrolysis of PPi and maintenance of low PPi levels is essential for all organisms. In animals, yeast, and bacteria, cytosolic soluble pyrophosphatase (sPPase) enzymes are solely engaged in PPi breakdown. In plant cells, the vacuolar proton pump PPase ($H^+$-PPase) is embedded in the vacuole membrane (the tonoplast) and functions to remove PPi from the cytosol and to pump protons into and acidify the vacuole. Although plants also have sPPases, their properties and physiological roles are not fully understood. However, the $H^+$-PPase-deficient mutant *fugu5* can grow normally, suggesting that other PPases may contribute to PPi hydrolysis in the cytosol.

**Question:** *Arabidopsis thaliana* has a single gene for vacuolar $H^+$-PPase (*VHP1/FUGU5/AVP1*) and five genes for cytosolic sPPase (*PPa1* to *PPa5*). We wanted to know which one is the major cytosolic sPPase and how these sPPases and $H^+$-PPase cooperatively maintain PPi concentration at proper levels in plant cells.

**Findings:** We analyzed sPPase knockout mutants of Arabidopsis but found no change in their growth, gross phenotype, and PPi concentrations. Interestingly, double knockout mutants of $H^+$-PPase and sPPase showed significant morphological changes and significant increase in PPi levels. Our findings indicate that $H^+$-PPase functions as a key PPi-hydrolysis enzyme and several sPPases also contribute to prevent increases in PPi concentrations to toxic levels in Arabidopsis. Cell walls of the double mutant *fugu5 ppa1*, displaying the most severe phenotypes, had low cellulose content and could not mechanically resist a hypotonic stress. Interestingly, *fugu5 ppa1* accumulated a lot of starch granules in plastids. It is suggested that high PPi levels change the metabolic flow from cell wall to starch synthesis.

**Next steps:** Although we demonstrated that sPPases function in plant cells, their physiological importance is still unclear. To pinpoint their roles more precisely, we will further investigate a quadruple mutant, *ppa1 ppa2 ppa4 ppa5*, which shows a clear phenotype, under a variety of growth conditions.

1987). Gene silencing of plastid *PPa6* in tobacco (*Nicotiana tabacum*) resulted in dynamic changes in chloroplast metabolism (George et al., 2010), suggesting that PPa6 is a major enzyme for PPi hydrolysis in plastids. Of the cytosolic isozymes, the overexpression of *PPa1* driven by a seed-specific promoter reduced seed oil content and increased starch and soluble sugar contents in Arabidopsis (Meyer et al., 2012). The reduced PPi levels in *PPa1*-overexpressing plants are thought to stimulate both the β-oxidation of stored lipids and sugar biosynthesis. By contrast, seed-specific silencing of *PPa1* and *PPa4* led to a 1 to 4% increase in seed oil contents (Meyer et al., 2012). Taken together, these findings indicate that sPPases strongly influence lipid and sugar metabolism in plants.

We recently reported that *AtVHP1/FUGU5/AVP1*, encoding a vacuolar $H^+$-PPase, regulates cytosolic PPi levels (Ferjani et al., 2011; Asaoka et al., 2016; Fukuda et al., 2016). Three independent VHP1 loss-of-function mutant lines (the *fugu5* mutant series) have been identified based on their gross phenotypes (including oblong-shaped cotyledons) and their cellular phenotypes (namely, compensation; i.e., cell enlargement due to a decrease in cell number) (Ferjani et al., 2007). This phenotype is caused by an increase in PPi levels, which inhibits the gluconeogenesis of seed storage lipids to sucrose (Ferjani et al., 2011; Takahashi et al., 2017). At the postgermination stage of development, *fugu5* mutants also exhibit moderately delayed growth, although they appear healthy (Asaoka et al., 2016; Fukuda et al., 2016). This contrasts with bacteria and yeast, in which loss of function of sPPase results in cell death (Chen et al., 1990; Serrano-Bueno et al., 2013). Therefore, it is important to evaluate the physiological balance between cytosolic sPPases and vacuolar $H^+$-PPase in plants.

In this study, we examined the expression of sPPase isozymes and their roles in PPi hydrolysis in Arabidopsis. We also characterized loss-of-function mutants of *PPa1*, *PPa2*, *PPa4*, and *PPa5*, together with various double knockout mutants of these sPPase isozyme genes and *fugu5*. Among the double mutants, a few combinations, such as *fugu5-1 ppa1-1*, displayed severe phenotypes, whereas single knockout mutants exhibited rather moderate phenotypes. Finally, we determined the PPi contents in mutant plant tissues. Together, our findings provide important information about the relationships among loss-of-function mutations, phenotypes, and PPi levels. We discuss the physiological cooperation between vacuolar $H^+$-PPase and sPPase isozymes in regulating cytosolic PPi levels.

## RESULTS

### Generation of Loss-of-Function Mutants of Cytosolic Soluble PPase Isozymes

To investigate the phenotypes of Arabidopsis mutants lacking each of the PPa isogenes, we obtained the following T-DNA insertion lines from the Nottingham Arabidopsis Stock Centre (http://arabidopsis.info): *ppa1-1*, SAIL_251_D07; *ppa2-1*, SAIL_618_H05; *ppa4-1*, SAIL_916_C08; and *ppa5-1*, SALK_014647. To confirm the insertion of T-DNA into the corresponding genes, we performed PCR using genomic DNA from each line with T-DNA- and gene-specific primers (Supplemental Figure 1). We also generated multiple knockout mutants through crosses: The quadruple mutant *ppa1-1 ppa2-1 ppa4-1 ppa5-1* is referred to as *ppa1,2,4,5* hereafter. The mutant lines were used for isozyme measurements and phenotypic analyses.

### Detection of Cytosolic PPa Isozymes

To detect PPa isozymes in tissues, we prepared microsomal and soluble fractions by ultracentrifugation and performed immunoblotting with an anti-PPa antibody raised against a sequence conserved among the five isozymes. An immunostained band was clearly detected in the soluble fraction from the wild type (Supplemental Figure 2A). A faint band was observed in the wild-type microsomal fraction but not in the fraction from the quadruple mutant *ppa1,2,4,5*. These results suggest that the anti-PPa antibody is useful for detecting PPa proteins and that PPa is found in the soluble fraction. Together with previous reports on GFP fusion analysis (Koroleva et al., 2005; Öztürk et al., 2014; Gutiérrez-Luna et al., 2016), these results confirm the presence of PPas in the cytosol.

The amino acid sequences of the five PPa isozymes are only 69% identical (Schulze et al., 2004), although these proteins have similar molecular masses (Supplemental Figure 2B). These differences in primary amino acid sequences suggest that it is possible to distinguish between each isozyme. We therefore separated the proteins by two-dimensional polyacrylamide gel electrophoresis (2D-PAGE) and detected them by immunoblotting (Supplemental Figure 2C). We identified spots corresponding to each PPa isozyme by comparing them with those from the wild type with multiple knockout lines, although we observed several nonspecific spots larger than 28 kD on the immunoblots. For PPa1 and PPa5, we detected two spots with different isoelectric point (pI) values (Supplemental Figure 2C). The lower pI spots might represent phosphorylated proteins, as the phosphorylation of plant sPPases has been reported (de Graaf et al., 2006; Eaves et al., 2017). The pI values of each spot were comparable to the calculated pI values of each isozyme. We failed to detect a spot corresponding to PPa3, with a calculated pI of 5.63 and a molecular mass of 24.9 kD in the wild type (Supplemental Figures 2B and 2C), suggesting that PPa3 is absent in vegetative tissues.

### Tissue Specificity of PPa Isozymes

To examine the tissue specificity of the PPa isozymes, we determined their relative abundance by immunoblotting with anti-PPa antibody. First, we compared the relative levels of PPa isozymes in roots and shoots at 16 d after sowing (DAS) and in other organs of 5-week-old plants (Figures 1A and 1B). PPa isozymes were detected at ~27 kD in all wild-type tissues. In 5-week-old plants, the total isozyme content was highest in flowers. We also examined samples from the quadruple mutant *ppa1,2,4,5* in parallel with the wild type but did not detect any bands corresponding to PPas (Figures 1A and 1B). These results point to the low abundance of PPa3 in these tissues.

Next, we compared the abundance of each PPa in individual single knockout mutant lines with that in the wild type by immunochemical analysis. Wild-type leaves and flowers showed intense bands, but the *ppa1* mutants exhibited faint bands (Figure 1C), confirming the abundance of PPa1 in leaves and flowers. PPa1 was also more abundant in shoot and root tissues than were the other isozymes.

PPa2 was abundant in buds and fruits, as indicated by the decreased immunoblot intensity for the *ppa2* mutants (Figure 1C). Shoots, roots, leaves, stems, and flowers also contained considerable amounts of PPa2. On the other hand, stems and buds contained substantial amounts of PPa4. For PPa5, the intensity of stained bands was slightly reduced in all tissues examined except roots and leaves. A spot clearly corresponding to PPa5 was detected by 2D-PAGE analysis (Supplemental Figure 2). Thus, PPa5 appears to be broadly expressed in most plant tissues at rather low levels. We could not examine PPa3 content in this study because no corresponding knockout mutant was available.

### Visualization of PPa Isozymes via the Expression of GFP Fusion Protein

To further investigate the spatiotemporal localization of PPa isozymes, we constructed GFP fusion proteins with PPa1, PPa2, PPa3, PPa4, and PPa5. To observe the natural endogenous expression patterns of these proteins, the constructs contained the promoters, introns, and 3′ untranslated regions (UTRs) of these genes. In this experiment, we used cfSGFP2 (hereafter, cfGFP), a cysteine-free GFP variant with strong green fluorescence (Suzuki et al., 2012). As discussed below, the expression of PPa1-cfGFP and PPa4-cfGFP rescued the *fugu5-1 ppa1-1* and *fugu5-1 ppa4-1* phenotypes, respectively, indicating that PPa-cfGFPs have enzymatic activity when expressed in seedlings and localize to the proper subcellular spaces (Supplemental Figure 3). All PPa-cfGFPs were detected in the cytosol and nucleus (Figures 2A to 2F). In the immunoblot analysis, no 27-kD band corresponding to free GFP, which can freely pass through nuclear pores, was detected, suggesting that the nucleus-localized signals were from genuine PPa-cfGFP (Figure 2G). The results of PPa-GFP spatiotemporal expression analysis are shown in Supplemental Figures 4 to 8 and are summarized in Table 1.

### PPa Isozyme Activity

The five cytosolic PPa isozymes share high sequence similarity, except for their N-terminal regions. The five isozymes share a sequence identity of 69% (Schulze et al., 2004). This high identity suggests that these isozymes share functional similarity, acting as pyrophosphatases in planta. PPa1 and PPa4 possess PPi hydrolysis activity, as revealed in an *E. coli* heterologous expression system (Navarro-De la Sancha et al., 2007). The enzymatic functions of PPa2, PPa3, and PPa5, however, have not been confirmed. We attempted to measure pyrophosphatase activity in soluble fractions prepared from plants by ultracentrifugation but did not detect any differences between the wild type (0.105 ± 0.004 [SE] units/mg protein, $n = 3$) and *ppa1,2,4,5* (0.102 ± 0.002 [SE] units/mg protein, $n = 3$). The detected activity was probably derived from vacuolar acid phosphatase (Veljanovski et al., 2006), and sPPase activity might be negligible compared with that of vacuolar acid phosphatase(s). Because the plant vacuole accounts for over 90% of the cell volume in mature tissues, cytosolic sPPase must be separated from the other abundant phosphatases, such as vacuolar acid phosphatases, prior to measurement. In addition, perhaps the PPa isozymes were inactivated during preparation of the soluble fractions from tissue homogenates.

Therefore, we analyzed the PPase activity of each PPa isozyme following expression in a transgenic yeast yTT1 strain in which the *Gal1* promoter was replaced by the promoter of the yeast

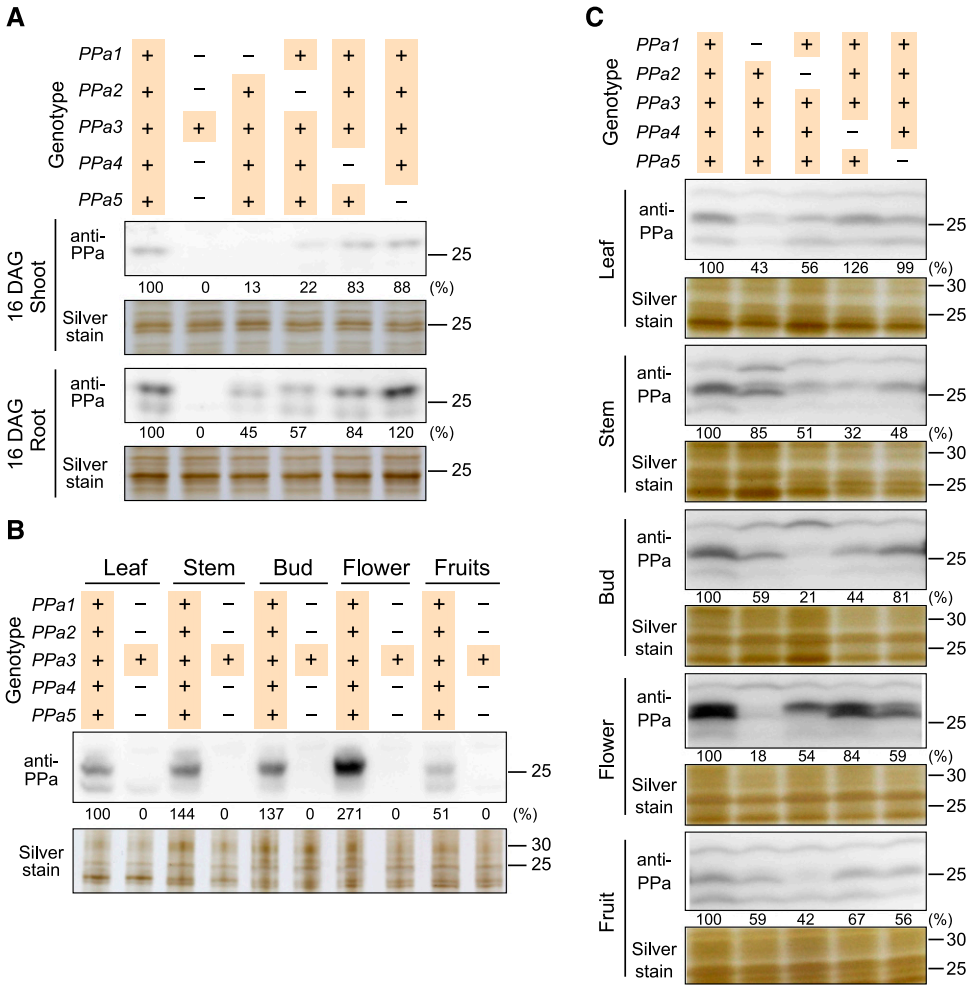


**Figure 1.** Tissue Specificity of Arabidopsis PPa Isozymes Detected by Immunoblotting.

The soluble fractions prepared from various organs of individual knockout lines and the quadruple *ppa1,2,4,5* mutant were immunoblotted with anti-PPa. The gels were also silver-stained to test the amount of protein loaded. Relative intensity of the immunoblot is shown as a percentage compared with the wild type (**[A]** and **[C]**) or leaves **(B)**.

**(A)** Relative quantities of PPa isozymes in the supernatants of homogenates prepared from shoots and roots of the wild type and five individual mutants at 16 DAS. The molecular masses of marker proteins are given on the right (kD).

**(B)** Relative amounts of PPa isozymes in leaves, stems, buds, flowers, and fruits of 37-DAS plants. Soluble fractions were prepared from the wild type and quadruple mutant *ppa1,2,4,5*.

**(C)** Comparison of PPa levels in five organs. Soluble fractions were prepared from the wild type and *ppa1-1*, *ppa2-1*, *ppa4-1*, and *ppa5-1* single mutants.

cytosolic sPPase gene *IPP1*. Arabidopsis *PPa* isogenes were introduced individually into yTT1 yeast cells under the control of the *IPP1* promoter. Although PPa levels varied among transformants, all yeast strains expressing PPa isozymes exhibited normal growth in glucose-based culture medium in which the expression of endogenous *IPP1* was strongly suppressed (Supplemental Figures 9A and 9B), indicating that these PPa isozymes possess PPase activity.

### Phenotypic Properties of Single and Multiple PPa Mutants, Particularly the *fugu5 ppa1* Double Mutant

The *ppa1,2,4,5* mutant showed no obvious phenotype (Figures 3 and 4). There are two possible explanations for this: (1) Cytosolic PPa isozymes may not contribute to PPi homeostasis or (2) perhaps there are other redundant pyrophosphatases that hydrolyze cytosolic PPi. To examine the physiological roles of vacuolar H+-PPase and cytosolic PPa isozymes in PPi homeostasis, we crossed the PPa knockout mutants with VHP1-deficient lines, *fugu5-1* and *fugu5-3*. The resulting double knockout mutants were all viable and fertile. Nonetheless, several double knockout mutants showed significant phenotypes in their roots and shoots (Figures 3 and 4; Supplemental Figure 10). In particular, the severe phenotype of *fugu5-1 ppa1-1* was also detected in the hypocotyls of etiolated seedlings. Notably, *fugu5-1 ppa1-1* showed severe defects in hypocotyl elongation in both the presence and absence of sucrose (Figures 5A and 5B).

The *fugu5*s *ppa1-1* lines (*fugu5-1 ppa1-1, fugu5-3 ppa1-1*) showed severe phenotypes (Figure 3; Supplemental Figure 10),

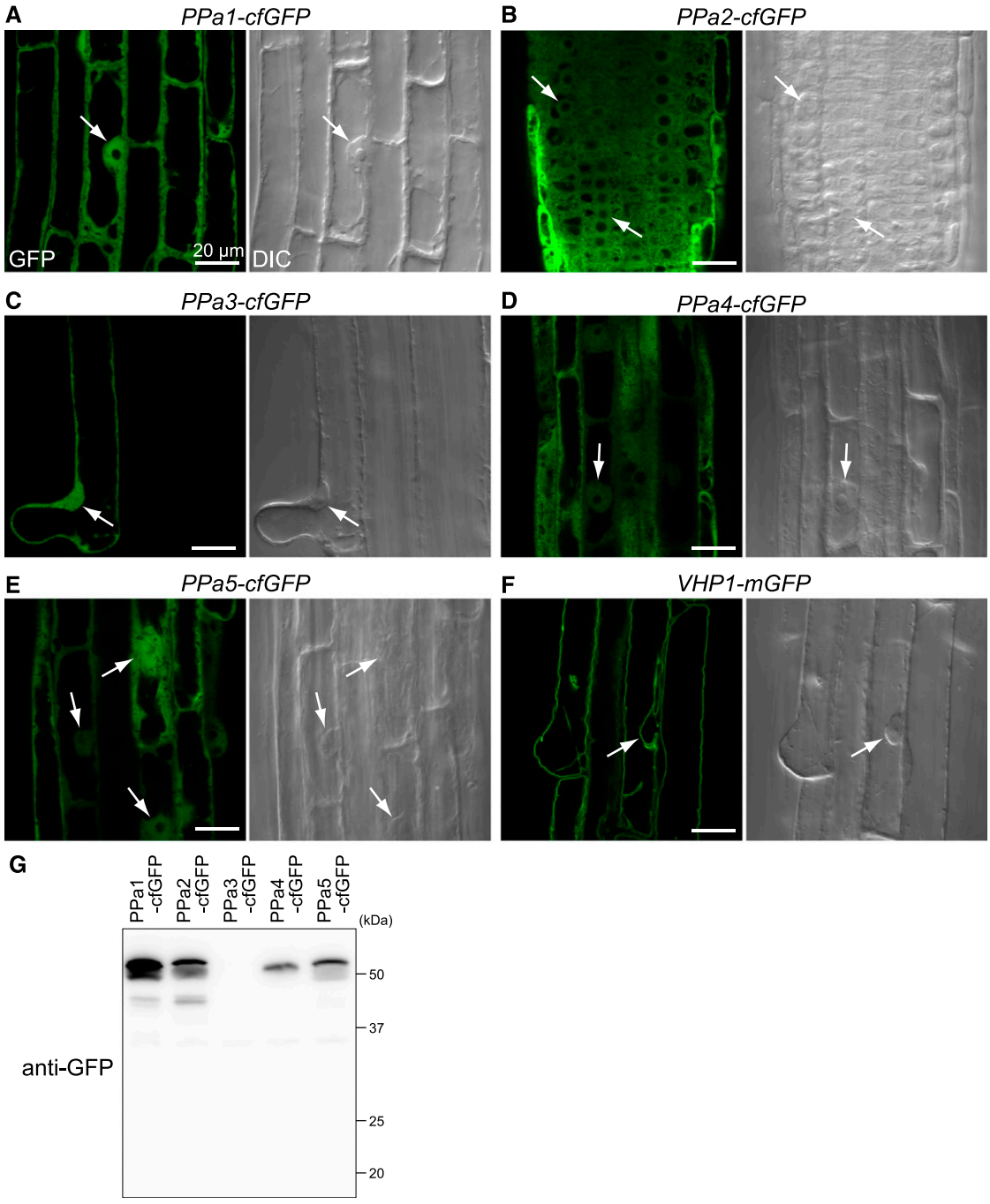


**Figure 2.** Subcellular Localization of PPa Isozymes.

**(A)** to **(F)** Roots expressing PPa1, PPa2, PPa3, PPa4, PPa5, or VHP1 fused with GFP under the control of their own promoters from plants grown for 6 to 21 d on 0.5× MS plates containing 1% sucrose were observed by CLSM. The root regions observed in the experiment were as follows: **(A)** PPa1-cfGFP line #14, elongation zone; **(B)** PPa2-cfGFP line #12, division zone; **(C)** PPa3-cfGFP line #16, root hairs; **(D)** PPa4-cfGFP line #11, differentiation zone; **(E)** PPa5-cfGFP line #5, differentiation zone; and **(F)** VHP1-mGFP line #wM-A9, differentiation zone. Arrows indicate nuclei. Green fluorescence from GFP-linked PPa isozymes was detected in the cytosol and nuclei. Bars = 20 μm.

**(G)** Immunochemical analysis of PPa-GFP protein. A 5-μg sample of the soluble fraction prepared from shoots of 20 DAS plants was immunoblotted with anti-GFP.

**Table 1.** Tissue Specificity of PPa Isozyme in Arabidopsis

| | | PPa1 | PPa2 | PPa3 | PPa4 | PPa5 | VHP1 |
|---|---|---|---|---|---|---|---|
| 3-DAS seedling (Supplemental Figure 4) | Cotyledon epidermis | + | ± | − | + | − | ++ |
| | Cotyledon stomata | ++ | ± | − | ++ | − | ++ |
| | Cotyledon mesophyll | ++ | + | − | − | − | ++ |
| | Hypocotyl | ++ | + | − | + | ± | ++ |
| | Vascular bundle | + | + | − | ++ | − | + |
| | Apical | + | + | − | ++ | ± | + |
| 4-DAS developing leaf (Supplemental Figure 4) | Epidermis | + | + | − | + | − | + |
| | Mesophyll | ± | ± | − | ± | − | + |
| | Trichome | ± | − | − | ++ | − | + |
| | Stipule | + | + | − | + | + | + |
| Mature leaf (Supplemental Figure 5) (VHP1 from Segami et al. [2014]) | Epidermis | + | ± | − | + | + (Petiole) | + |
| | Stomata | + | ± | − | + | ± | + |
| | Trichome | + | − | − | ++ | + | ++ |
| | Mesophyll | ++ | + | − | − | − | ++ |
| Root (Supplemental Figure 6) | Columella 1,2 | + | ++ | − | ± | − | − |
| | Columella 3,4 | + | ++ | − | + | + | ++ |
| | Lateral root cap | + | + | − | + | + | + |
| | Stem cell | + | ++ | − | + | − | ± |
| | Division | + | + | − | + | − | ++ |
| | Elongation | + | ± | − | + | ± | ++ |
| | Differentiation cortex | + | ± | − | ± | − | + |
| | Differentiation non-hair cell | + | ± | − | + | + | + |
| | Differentiation hair cell | + | ± | + | ± | + | + |
| | Vascular bundle | + | + | − | ++ | − | + |
| Flower (Supplemental Figure 8) | Pollen | ++ | ± | ++ | − | ++ | + |
| | Carpel | ++ | + | − | + | + | ++ |
| | Placenta | + | ++ | − | ++ | ± | ++ |
| | Pollen sac | + | + | − | ++ | + | ++ |
| | Stamen | + | ++ | − | + | + | + |
| | Petal | + | + | − | + | + | + |
| | Sepal | + | + | − | + | + | + |
| | Nectary | + | ± | − | ± | ++ | ++ |
| | Petal | + | ++ | − | ± | ++ | + |
| | Stamen | + | ++ | − | ± | + | + |
| Etiolated hypocotyl (Supplemental Figure 7) | Hock | ++ | + | − | + | − | ++ |
| | Middle | + | − | − | + | − | + |
| | Vascular bundle | ± | + | − | ++ | − | ± |

The relative expression of each isozyme in tissues is classified based on the intensity of fluorescence from GFP fusion proteins. ++, Extremely high fluorescence; +, easily detected; ±, weak fluorescence; −, not detected.

although the other mutants grew as well as the wild type on medium containing 1% sucrose. The growth of *fugu5*s *ppa1-1* was markedly suppressed on sucrose-free medium and did not totally recover upon sucrose supplementation (Figures 3A to 3C; Supplemental Figure 10). The rosette leaves of *fugu5*s *ppa1-1* and *fugu5*s *ppa4-1* plants showed symptoms of atrophy, a phenotype that did not recover upon the addition of sucrose.

The roots of *fugu5-1 ppa1-1* and *fugu5-1 ppa2-1* were short and thick, with an increased number of root hairs (Figure 4), as were the roots of *fugu5-3 ppa1-1* and *fugu5-3 ppa2-1* (Supplemental Figure 10). The meristematic and elongation zones of *fugu5-1 ppa1-1* roots were extremely short; sucrose supplementation in the growth medium enhanced the root phenotype of this double mutant (Figures 4B and 4C). We performed a complementation assay and found that introducing the genomic sequences of *PPa1*, *PPa2*, and *PPa4* completely rescued the phenotypes of the individual mutants (Supplemental Figure 11). The *fugu5-1 ppa1-1* mutant was also rescued by the expression of yeast *IPP1* (Figures 4E and 4F). These results suggest that PPa isozymes function as pyrophosphatases in vivo and that their loss of function in the *fugu5* background caused the phenotypes mentioned above.

### Marked Increases in PPi Accumulation in *fugu5 ppa1* Double Mutants

We examined whether the lack of H+-PPase and PPa isozymes further increases PPi levels in plants. The PPi content in the single mutant, *fugu5-1* (51.6 nmol/g fresh weight [FW]), was greater than that of the wild type (31.5 nmol/g FW) (Figure 5C), which is consistent with our previous finding (Ferjani et al., 2011). Although the PPi content in *ppa1-1* (30.1 nmol/g FW) was comparable to that of the wild type, the PPi content was significantly higher in

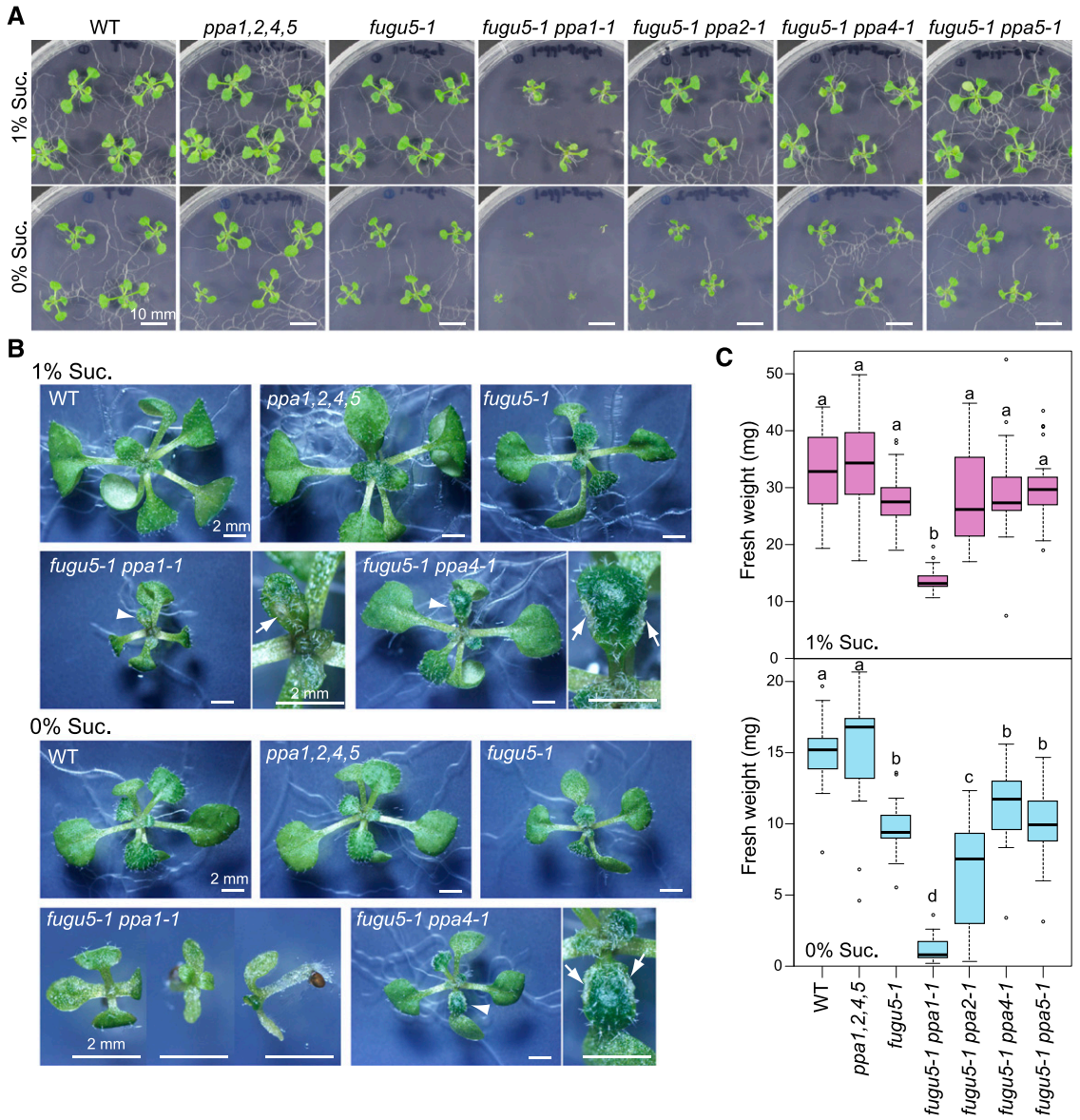


**Figure 3.** Phenotypes of Multiple Knockout Mutants of PPa and H$^+$-PPase in Shoots.

**(A)** and **(B)** Plants grown on 0.5× MS plates containing 1% sucrose or no sugar were captured with a digital camera **(A)** or a stereomicroscope **(B)** at 13 DAS. Arrowheads indicate leaf atrophy, and magnified images are also shown on the right. Bars = 10 mm in **(A)** and 2 mm in **(B)**. Arrows indicate atrophied areas **(B)**. **(C)** Fresh weights of whole plants. The box plot was created using R version 3.1.2, and different letters above each bar indicate statistically significant differences ($P < 0.05$, Tukey's HSD test; R version 3.1.2). $n = 15$ to 21 from three independent biological replicates.

*fugu5-1 ppa1-1* (197 nmol/g FW) than in *fugu5-1*. These results indicate that H$^+$-PPase is essential for maintaining adequate PPi levels and that the cytosolic PPa isozymes, particularly PPa1, prevent increases in PPi concentrations to toxic levels.

The sucrose content in *fugu5* seedlings is low due to suppressed gluconeogenesis (Ferjani et al., 2011; Takahashi et al., 2017). The sucrose content per seedling in *fugu5-1 ppa1-1* was lower than in the wild type but slightly higher than in the *fugu5-1* single mutant (Figure 5D). Based on fresh weight, the sucrose content was highest in *fugu5-1 ppa1-1* and lowest in *fugu5-1*.

Triacylglycerol (TAG) is the main energy and carbon source in germinating seedlings. In dry seeds, all mutants had normal TAG contents; however, in 3-DAS etiolated seedlings, TAG levels were significantly higher in *fugu5-1 ppa1-1* than in the other lines (Figure 5C). These results suggest that excess PPi levels delay the breakdown of TAG.

### Morphological Defects in the Cell Walls of *fugu5 ppa1* Roots

The severe growth suppression of *fugu5*s *ppa1-1* roots prompted us to investigate morphological changes in mutant root tissues.

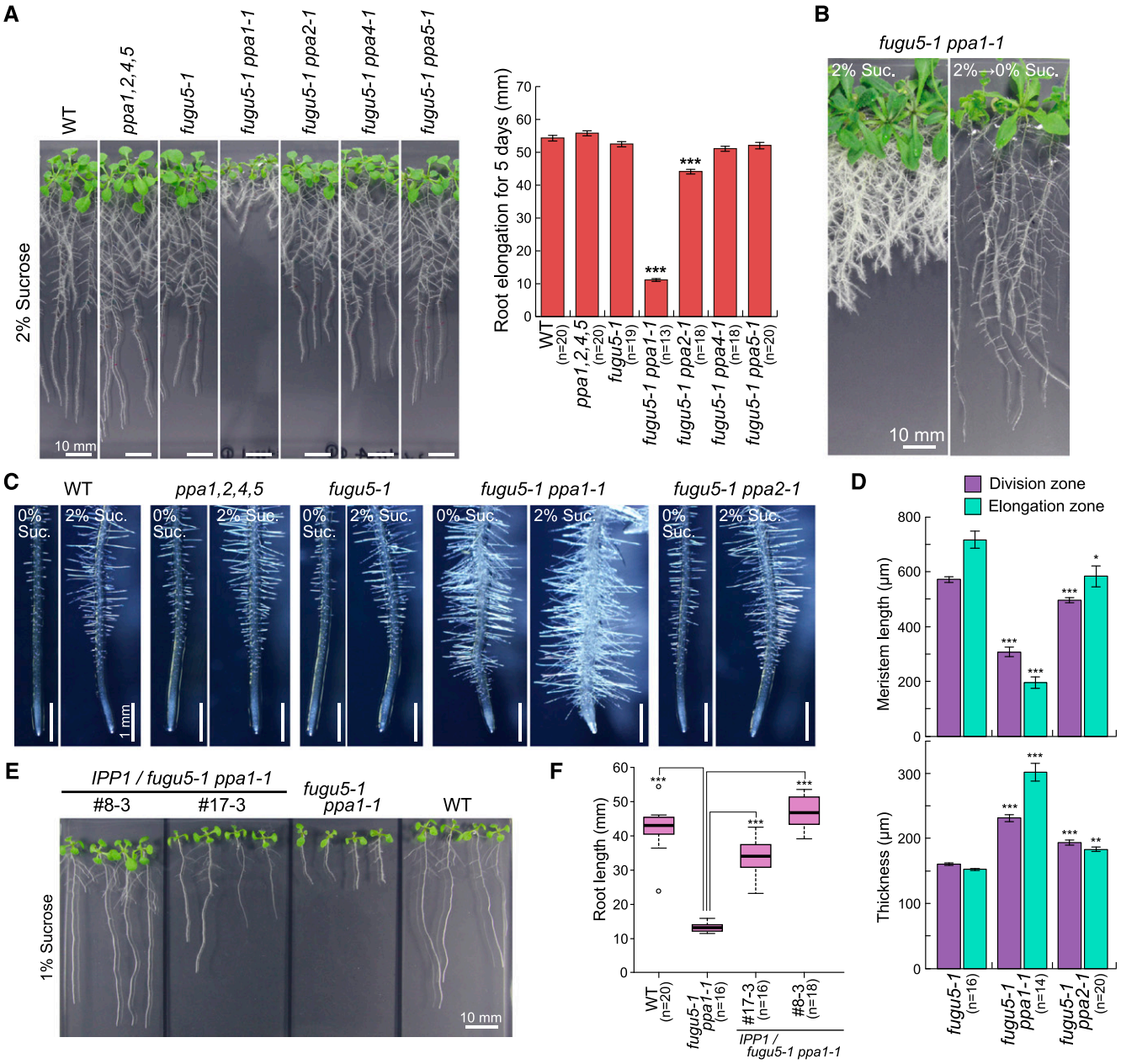


**Figure 4.** Root Phenotypes of Multiple PPa and H+-PPase Knockout Mutants.

**(A)** Root lengths of seedlings grown on 0.5× MS plates with 2% sucrose for 13 d. Measurements taken after 5 d (from day 8 to day 13) are shown. Bars = 10 mm.

**(B)** *fugu5-1 ppa1-1* was grown on a 0.5× MS/2% sucrose plate for 6 d, transferred to a sugar-free plates, and grown for 18 d.

**(C)** Stereomicroscopic analysis of roots, including the root tip. Bars = 1 mm.

**(D)** Comparison of root tip length and thickness of *fugu5-1*, *fugu5-1 ppa1-1*, and *fugu5-1 ppa2-1* grown on 2% sucrose plates for 9 d. Dv, cell division zone; El, elongation zone. One border was set between the cell division and elongation zones where the first square cortex cell was observed, and the other border was set between the elongation and maturation zone where the first root hair bulge was observed. Error bars indicate SE. Asterisks indicate significant differences at *P < 0.05, **P < 0.01, and ***P < 0.001 compared with *fugu5-1* (Tukey's HSD test; R version 3.1.2).

**(E)** and **(F)** Complementation of *fugu5-1 ppa1-1* by yeast sPPase gene *IPP1*.

**(E)** Vertical-plate culture of *fugu5-1 ppa1-1* harboring *IPP1*. The line numbers (#8-3 and #17-3) correspond to the transgenic *IPP1* parental lines (*AVP1*$_{pro}$:*IPP1*; Ferjani et al., 2011).

**(F)** Comparison of root length in mutants grown for 9 d. Asterisks indicate statistically significant differences at ***P < 0.001 (Tukey's HSD test; R version 3.1.2).

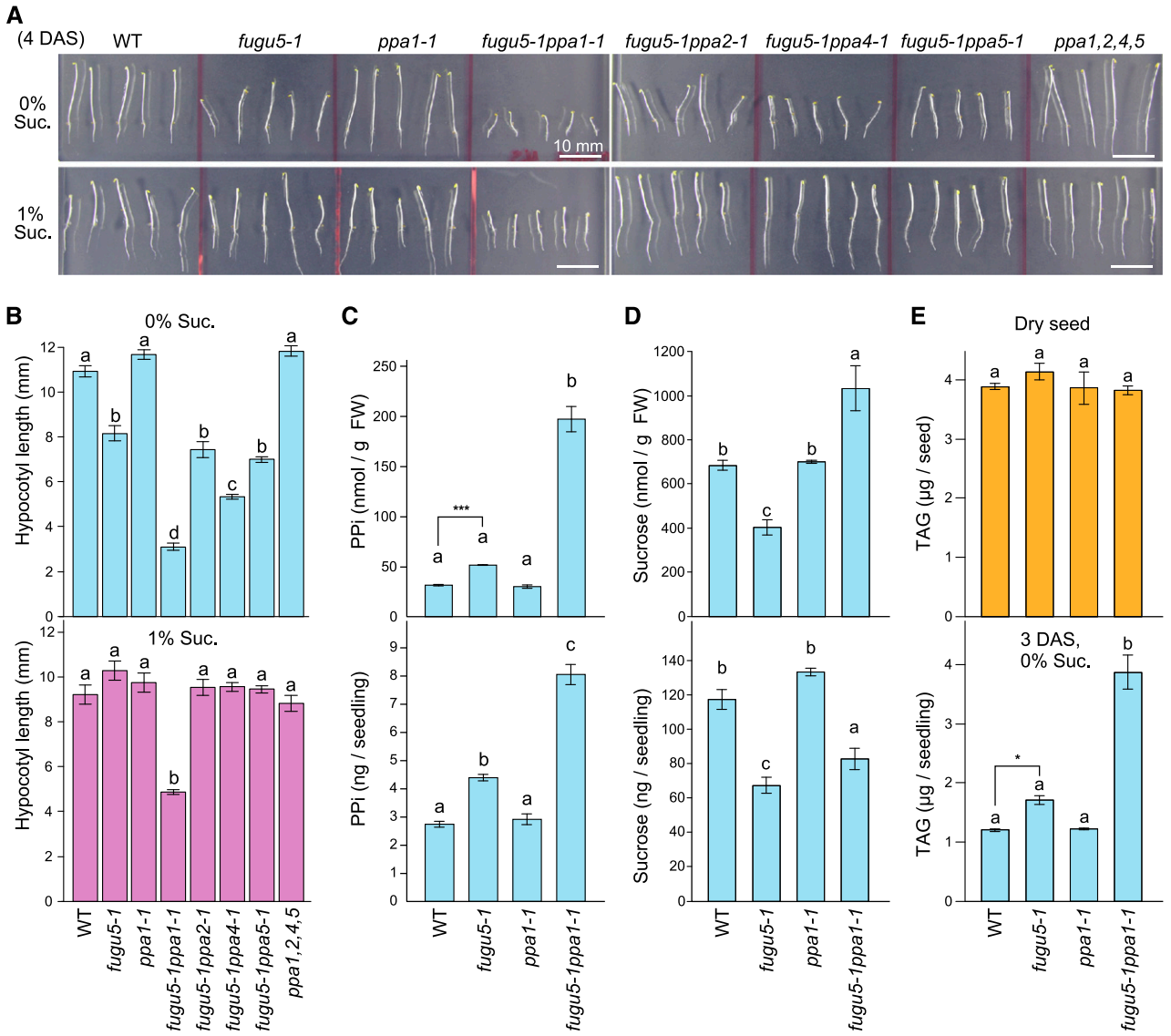


**Figure 5.** Defect in Hypocotyl Elongation in Multiple PPase Knockout Mutants.

Seeds were grown in the light for 6 h and transferred to the dark.

**(A)** Image of 4-DAS etiolated seedlings. Bars = 10 mm.

**(B)** Hypocotyl length in 4-DAS etiolated seedlings grown without sugar (upper) or with 1% sucrose (lower). Different letters above each bar indicate statistically significant differences ($P < 0.01$, Tukey's HSD test; R version 3.1.2). $n = 13$ to 15.

**(C)** PPi content in 3.5-DAS etiolated seedlings.

**(D)** Sucrose content in 3.5-DAS etiolated seedlings.

**(E)** TAG content in 3-DAS etiolated seedlings.

**(C)** to **(E)** Data are means and SE from three independent experiments. Letters indicate groups divided by Tukey's HSD test (R version 3.1.2). Asterisks indicate significant differences at *$P < 0.05$ and ***$P < 0.001$ compared with the wild type (Student's *t* test; R version 3.1.2).

In plants grown under normal conditions with sucrose, the epidermal and cortex cells of *fugu5 ppa1-1* roots were short and swollen, particularly elongating cells (Figure 6E). These characteristics resembled those of wild-type roots treated with the cellulose synthase inhibitor isoxaben (Xu et al., 2008; Figure 6B).

Electron microscopy analysis revealed defects in cell wall morphology in *fugu5-1 ppa1-1* roots. Parts of the horizontal cell walls in dividing cells appeared to be incomplete (Figures 6I and 6J). These incomplete cell walls were also detected in *fugu5-1 ppa1-1* roots by confocal laser scanning microscopy (CLSM) (Figure 6E, asterisks).

In addition, the cell walls of *fugu5-1 ppa1-1* roots showed a phenotype that could be interpreted as mechanical weakness. Indeed, when we immersed the roots of *fugu5-1 ppa1-1* plants

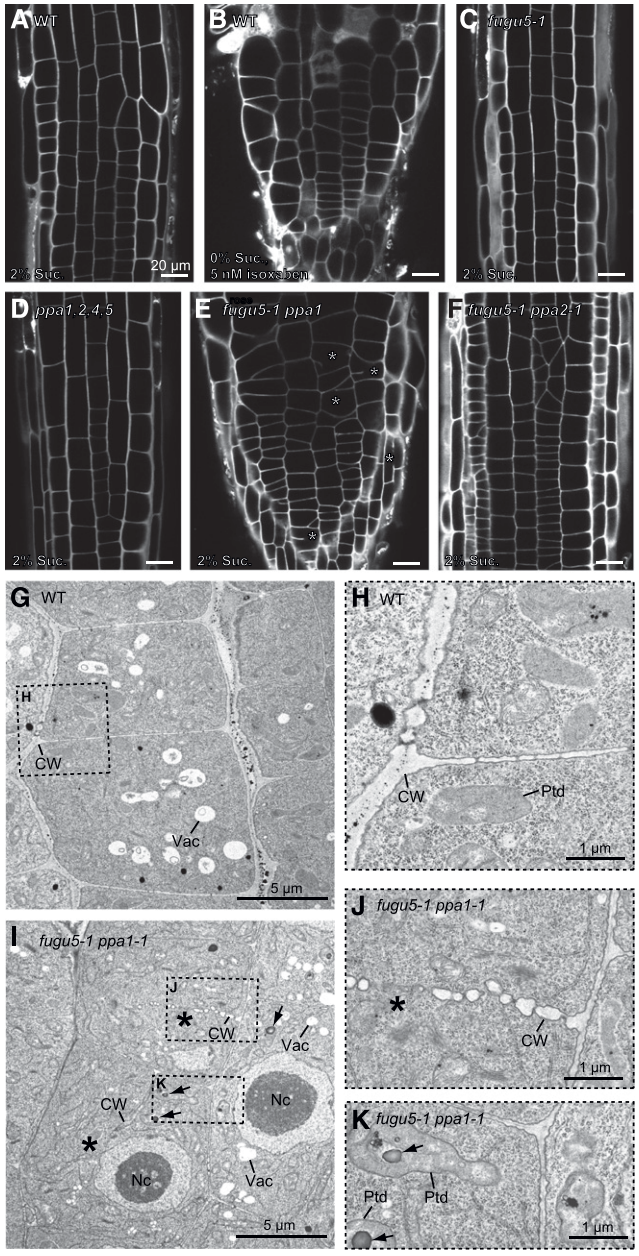


**Figure 6.** *fugu5-1 ppa1-1* Root Tips Exhibit Cell Swelling and Incomplete Cell Walls.

**(A)** to **(F)** CLSM analysis of the root elongation zone after staining cell walls with PI/0.25 M sorbitol. Bars = 20 μm.

**(G)** to **(K)** TEM images of the division zone in the root tip.

**(H)**, **(J)**, and **(K)** Enlarged images corresponding to the boxed regions in **(G)** and **(I)**.

Asterisks indicate incomplete cell walls, and arrows indicate starch grains. CW, cell wall; Ptd, plastid; Nc, nucleus; Vac, vacuole.

grown on 0.5× Murashige and Skoog (MS) culture medium in water containing propidium iodide (PI), their root tip cells swelled and burst within a few minutes (Figure 7A; Supplemental Movie 1). This bursting occurred after collapse of the inner root cells, which was clearly visible after PI staining (Supplemental Movie 2). When cellulose synthesis was inhibited in wild-type seedlings by 5 nM isoxaben treatment, the root tips of these seedlings were also swollen and damaged but did not burst (Figure 7B; Supplemental Movies 3 and 4). The *fugu5-1* and *ppa1-1* single mutants were not damaged by water immersion (Figure 7C). To examine whether the cells burst due to low osmotic pressure or other factors, we transferred *fugu5-1 ppa1-1* roots from 0.5× MS to PI staining solution containing various concentrations of sorbitol. Damaged PI-stained cells were observed in solutions containing ≤75 mM sorbitol (Figure 7D). Under 50 mM sorbitol treatment, half the area of the root tip was damaged. The osmotic pressure of 0.5× MS medium is ~80 mOsm. Thus, *fugu5-1 ppa1-1* root tips were sensitive to small reductions in osmotic pressure. These results suggest that a defect in cell wall synthesis reduces osmotic stress tolerance in roots.

### Changes in Cell Wall Composition in *fugu5-1 ppa1-1*

To further investigate the weakness of *fugu5-1 ppa1-1* cell walls, we used three different dyes to stain various cell wall components. The first dye, Direct Fast Scarlet 4BS, also known as Pontamine Fast Scarlet 4B (S4B; CAS no. 3441-14-3), specifically stains cellulose (Anderson et al., 2010). Although S4B cannot penetrate the surfaces of living roots, fixed samples were evenly stained by this dye, including inner root cells. S4B staining was notably weaker in *fugu5-1 ppa1-1* compared with the wild type, especially on the outside surface of the epidermis (Figures 8A and 8B), where thick cell walls were observed (Supplemental Figures 12D and 12E), compared with inner root cells (Figures 6G and 6I). Quantification of the intensity of staining showed that *fugu5-1 ppa1-1* was stained by S4B at a level only 17.6% that of the wild type. In addition, in another mutant with defective roots, *fugu5-1 ppa2-1*, the intensity of S4B staining was only 57.1% that of the wild type (Figures 8C and 8D; Supplemental Figure 12).

The second dye, Ruthenium Red, specifically stains pectin (Sterling, 1970). In contrast to S4B, Ruthenium Red staining was not significantly reduced in *fugu5-1 ppa1-1* versus the wild type (Figures 8E and 8F). The third dye, Aniline Blue, is used to stain β1,3-glucans including callose. Cell plates were clearly stained in the wild type (Figure 8G), whereas fewer stained cell plates, with lower signal intensity, were detected in *fugu5-1 ppa1-1* compared with the wild type (Figure 8H). In addition, 3D reconstructions of cell plates showed that callose was unevenly deposited in *fugu5-1 ppa1-1* (Figures 8G and 8H, bottom).

To further investigate differences in cell wall composition between *fugu5-1 ppa1-1* and the wild type, we examined the monosaccharide composition in alcohol-insoluble residue (AIR) extracted from the tissue, which contains cell wall materials and starch. In this analysis, we used hydroponically grown etiolated seedlings to avoid contamination by agar in the medium. As shown in Figure 9, compared with the wild type, *fugu5-1 ppa1-1* had lower ratios of non-starch Glc per total detected monosaccharides (found in cellulose and hemicellulose), GalA, and Gal (found in pectin), Xyl and Man (found in hemicellulose), and GlcA, Fuc, and mGlcA (found in hemicellulose and pectin). By contrast, the levels of Rha and Ara (found in pectin) were higher in *futu5-1 ppa1-1* than in the wild type. The results support the finding that *fugu5-1 ppa1-1* had less cellulose

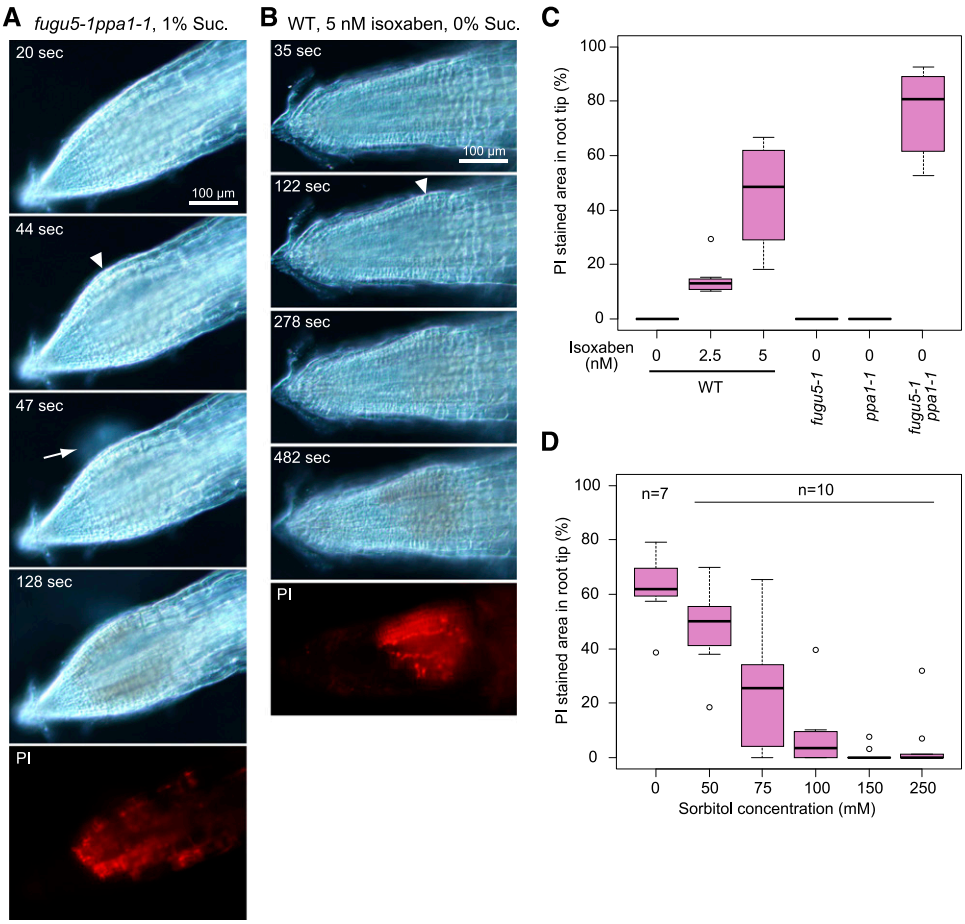


**Figure 7.** *fugu5-1 ppa1-1* Root Tip Cells Burst Due to Low Osmotic Pressure.

**(A)** and **(B)** Time-lapse imaging of water-submerged root tips. Root tips of *fugu5-1 ppa1-1* plants **(A)** grown on 0.5× MS medium with 1% sucrose and wild-type plants **(B)** treated with 5 nM isoxaben for 3 d on 0.5× MS medium without sucrose and transferred to water containing 10 μM PI. Arrowhead indicates a bulge caused by internal expansion. Arrow indicates a ruptured cell. After treatment, the root tip began to turn brown.
**(C)** Ratio of the injured versus noninjured area in the root division zone in plants transferred to water containing 10 μM PI.
**(D)** Ratio of the injured versus noninjured area in *fugu5-1 ppa1-1* root tips transferred to various concentrations of sorbitol.

than the wild type and are consistent with the results of imaging analysis. Imaging analysis revealed no marked difference in pectin (mainly composed of GalA, Gal, Rha, and Ara) content between the wild type and mutant. However, the pectin composition in *fugu5-1 ppa1-1* might be altered, with low homogalacturonan and high rhamnogalacturonan content, as indicated by the changes in monosaccharide contents in this mutant (Figure 9).

### Ectopic Accumulation of Starch in *fugu5 ppa1* Cells

In addition to the abovementioned changes, an analysis of monosaccharide composition in AIR revealed a marked increase in starch levels in etiolated *fugu5-1 ppa1-1* seedlings compared with the wild type (Figure 9). In addition, transmission electron microscopy (TEM) images of *fugu5-1 ppa1-1* roots show small starch grains with high electron density in plastids (Figures 6I and 6K, arrows). To test whether these were starch grains, we stained *fugu5-1 ppa1-1* roots with iodine. Columella cells in the root tip contain starch grains, which are involved in gravity sensing. We detected intense iodine staining in wild-type, *fugu5-1*, and *ppa1-1* root tips, particularly in columella cells (Figure 10A). Interestingly, *fugu5-1 ppa1-1* roots showed dense staining in the upper meristematic and transition zones, in addition to columella cells. These findings support the notion that the electron-dense grains in TEM images of *fugu5-1 ppa1-1* roots are likely starch grains, and they reveal extensive ectopic accumulation of starch in the root cells of the double mutant.

We also observed ectopic starch accumulation in other organs of *fugu5-1 ppa1-1*. In the wild type, *fugu5-1*, and *ppa1-1*, etiolated hypocotyls were stained with iodine, especially in the hook region. In the wild type and *ppa1-1*, only endodermal cells were stained, whereas *fugu5-1* showed starch grains in other cells as well, such as cortical cells. In *fugu5-1 ppa1-1* hypocotyls, the staining intensity was extremely high (Figure 10B). By contrast, in the third to fourth leaves of wild-type, *fugu5-1*, and *ppa1-1* plants grown in the dark and then illuminated for 2 h, only a few chloroplasts were slightly stained with iodine. In the third to fourth leaves of *fugu5-1*

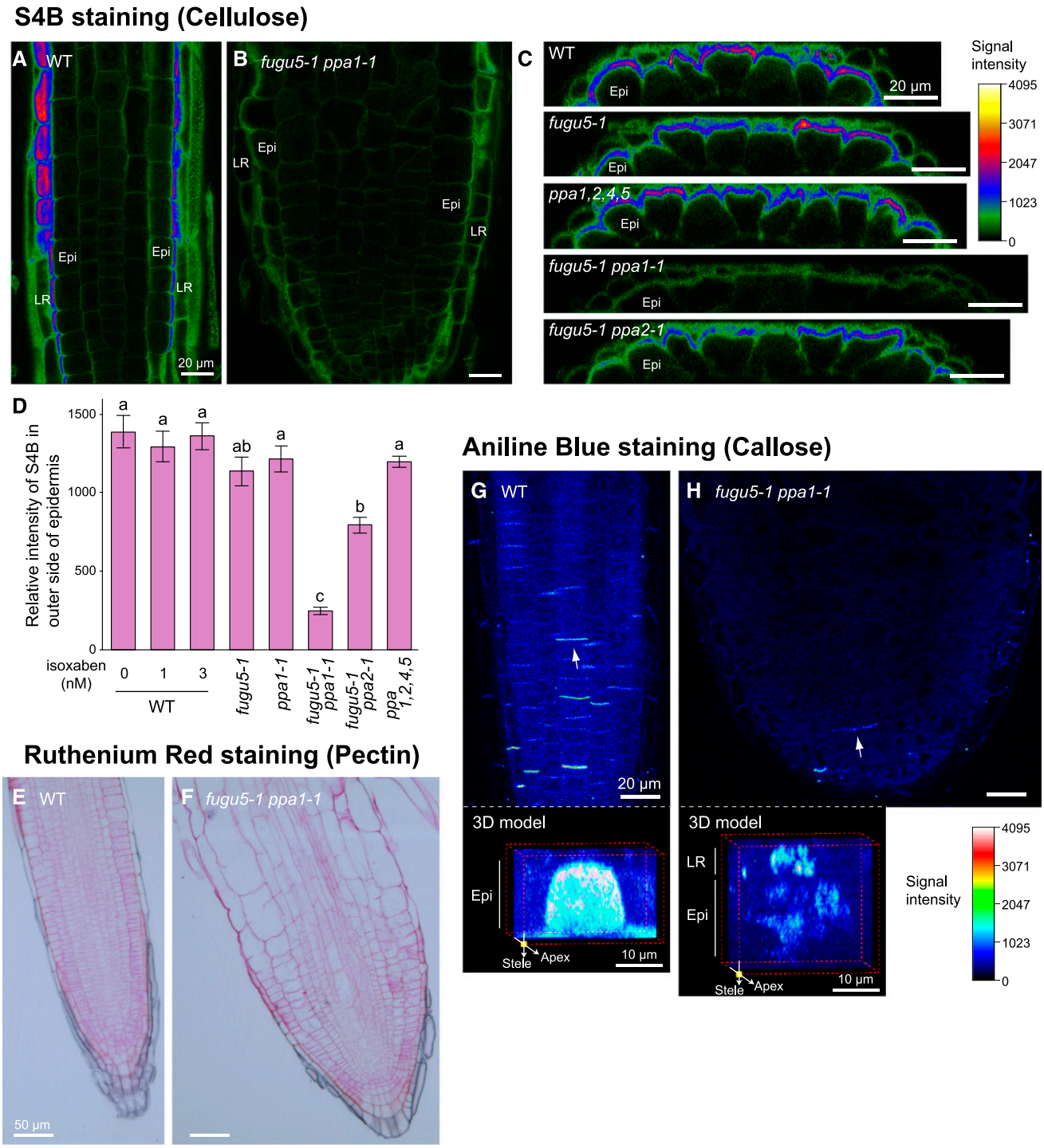


**Figure 8.** Staining of Cell Wall Components in the Root Tip.

Plants were grown on 0.5× MS medium containing 1% sucrose.

**(A)** to **(D)** CLSM analysis of S4B-stained root elongation zone. Roots of 8 DAS seedlings were fixed and cleared with ClearSee.

**(A)** and **(B)** X-Y images of root elongation zones taken 14 μm below the surface.

**(C)** X-Z images of root elongation zones. Bars = 20 μm.

**(D)** Quantification of S4B signal intensity between the lateral root cap and epidermis. Values were determined from Figure 8C, Supplemental Figure 12C, and their biological replicates. Error bars indicate SE ($n = 6$). Different letters above each bar indicate statistically significant differences ($P < 0.01$, Tukey's HSD test; R version 3.1.2).

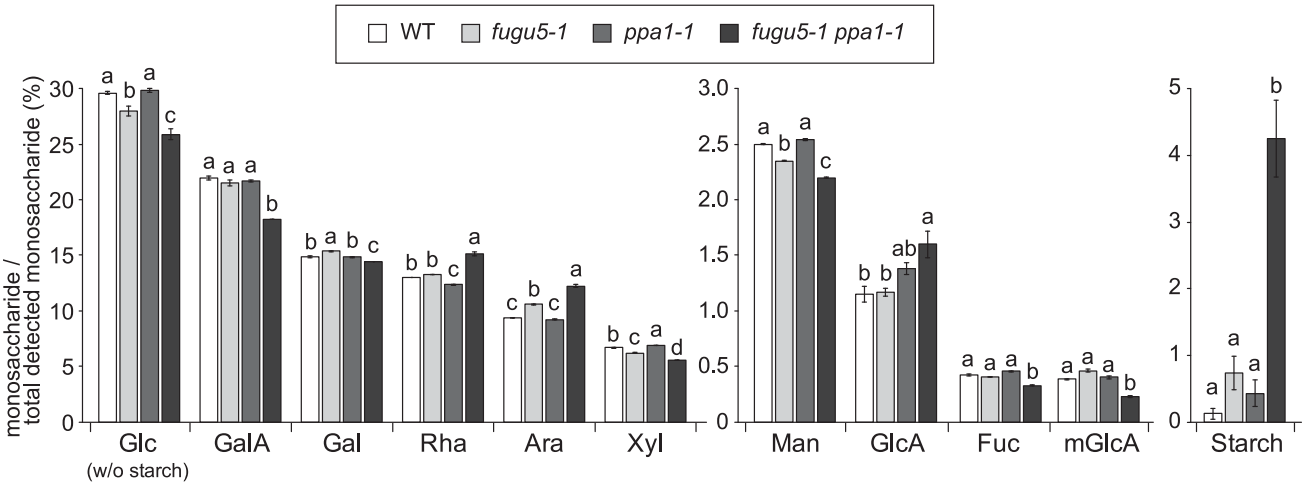


**Figure 9.** Monosaccharide Composition in 3-DAS Etiolated Seedlings.

The data are presented as monosaccharide content per total detected monosaccharides in AIR. Glucose (Glc), galacturonic acid (GalA), galactose (Gal), rhamnose (Rha), arabinose (Ara), xylose (Xyl), mannose (Man), glucuronic acid (GlcA), fucose (Fuc), and 4-*O*-methyl glucuronic acid (mGlcA). Error bars indicate SE ($n$ = 3). Different letters above each bar indicate statistically significant differences ($P < 0.05$, Tukey's HSD test; R version 3.1.2).

*ppa1-1*, however, whole leaves, including petioles, were densely stained (Figure 10C). Together, these results reveal high starch synthesis activity in leaves and a shift in energy metabolism from cell proliferation and elongation, including cellulose synthesis, to starch synthesis in the hypocotyl and elongating root cells of *fugu5-1 ppa1-1*.

## DISCUSSION

### Tissue Specificity and Abundance of PPa Isozymes

In this study, we established the cytosolic PPa knockout mutants *ppa1-1*, *ppa2-1*, *ppa4-1*, and *ppa5-1* and used them to examine the tissue specificity of each isozyme (Supplemental Figure 1). We investigated the presence of these isozymes in wild-type plants by immunoblotting (Supplemental Figure 2) and successfully detected the accumulation of GFP-tagged PPa isozymes expressed under the control of their own promoters (Table 1; Supplemental Figures 4 to 8). PPa1, PPa2, and PPa4 were found in cotyledons, hypocotyls, leaves, roots, and flowers, whereas PPa3 was only found in root hairs and pollen. CLSM analysis clearly revealed the presence of PPa5-GFP in mature epidermal cells in both shoots and roots (Supplemental Figures 5 and 6), but not in cotyledons (Supplemental Figure 4F), emerging rosette leaves (Supplemental Figure 4L), or the root elongation zone (Supplemental Figure 6). The low abundance of PPa5 in these developing tissues might be related to the observation that *fugu5*s *ppa5-1* showed no morphological phenotypes (Figures 3 and 4; Supplemental Figure 10). Furthermore, heterologous expression of these isozymes in yeast cells confirmed the PPi hydrolysis activity of PPa2, PPa3, and PPa5 (Supplemental Figure 9) in addition to PPa1 and PPa4 (Navarro-De la Sancha et al., 2007).

### Localization of PPa Isozymes in the Cytoplasm and Nuclei

The cytosolic localization of Arabidopsis PPa isozymes has been examined in plants expressing GFP-PPa (Koroleva et al., 2005; Öztürk et al., 2014; Gutiérrez-Luna et al., 2016). However, the results differ among reports. In our system, all cfGFP-fused PPa isozymes were detected in the cytosol and nucleus (Figure 2). We used a flexible linker, [$Gly_4Ser$]x3, and a cysteine-free monomeric GFP, cfGFP, which prevents the artificial formation of disulfide bonds and noncovalent dimer formation (Suzuki et al., 2012). These PPa-GFP chimeric proteins had enzymatic activity and were localized to their original subcellular compartments, confirming that PPa1-cfGFP and PPa4-cfGFP rescued the *fugu5-1 ppa1-1* and *fugu5-1 ppa4-1* phenotypes, respectively (Supplemental Figure 3). The dual localization of PPa isozymes in the cytosol and nuclei makes them physiologically effective in hydrolyzing PPi in both intracellular compartments, since the nucleus generates large amounts of PPi during gene transcription and DNA replication.

We will discuss the physiological roles of PPa isozymes based on their tissue specificity and localization in the cytosol and nuclei.

**Figure 8.** (continued).

**(E)** and **(F)** Light microscopy of roots tips stained with Ruthenium Red. The 5-DAS roots were cut into 5-μm-thick sections. Bars = 50 μm.
**(G)** and **(H)** CLSM analysis of Aniline Blue-stained root division zones. Roots were fixed and cleared with ClearSee. The images show at the bottom are 3D constructions of the cell plates indicated by arrows. Configuration of the CLSM and staining conditions were the same among samples. Epi, epidermis; LR, lateral root cap; CW, cell wall.

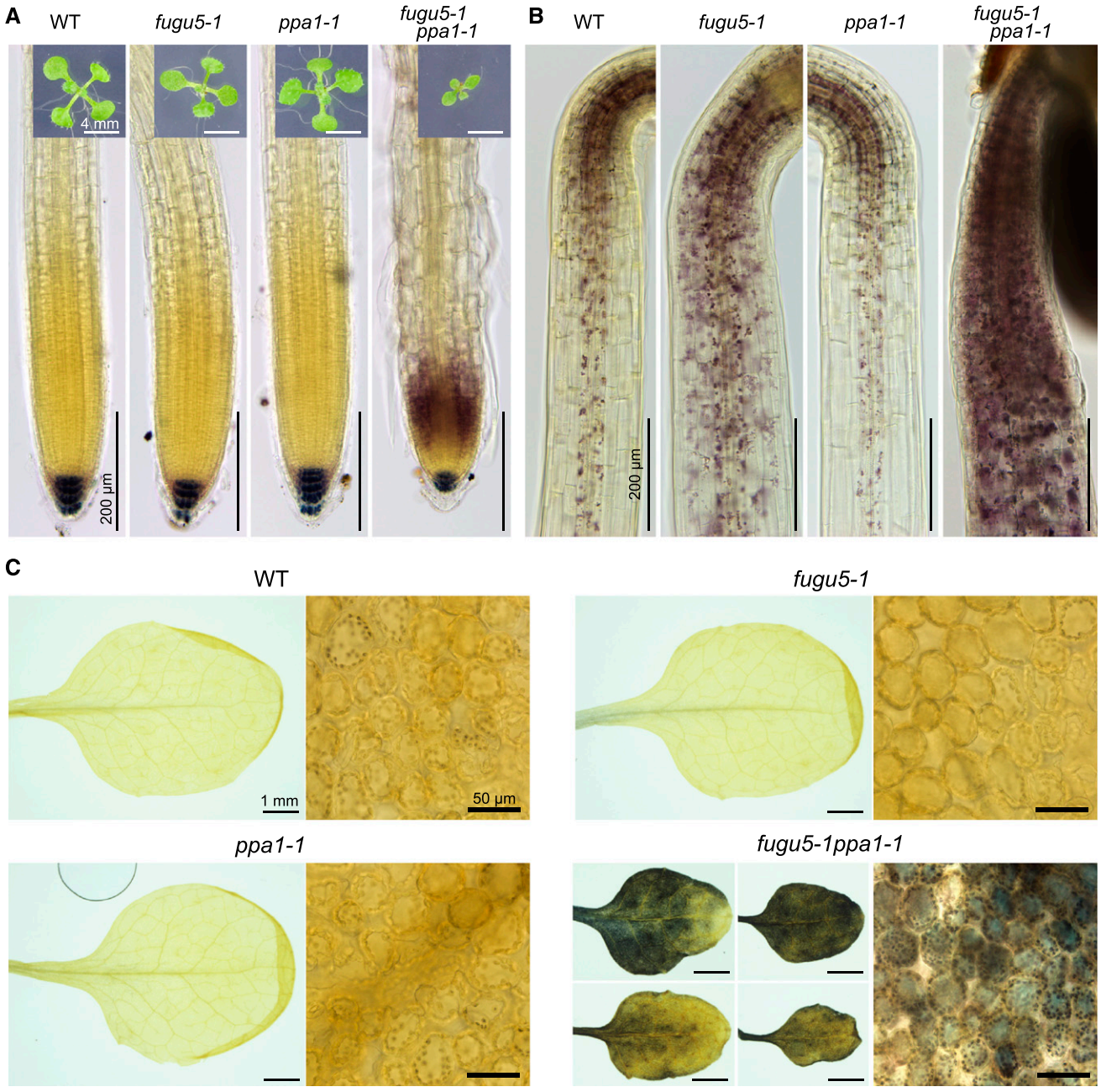


**Figure 10.** Ectopic Accumulation of Starch Grains in *fugu5-1 ppa1-1*.

Samples were fixed, cleared with ClearSee (Kurihara et al., 2015), and stained with iodine. Starch grains were stained blue, purple, or red depending on the chain length of amylose (Bailey and Whelan, 1961). All plants were grown in the absence of sucrose.
**(A)** Root tips of 2-week-old plants subjected to 8 h of illumination prior to fixation.
**(B)** 3-DAS etiolated hypocotyls.
**(C)** Iodine staining of third or fourth leaves after 2 h of illumination.

### Physiological Importance of PPa Isozymes, as Indicated by Their Knockout Mutants

The *fugu5*s *ppa1-1* mutant showed a severe phenotype in roots, with extremely short main roots, a short, thick meristem region, and numerous root hairs (Figure 4; Supplemental Figure 10). Roots of the *fugu5 ppa2-1* mutant showed a similar but milder phenotype compared with *fugu5 ppa1-1*. These phenotypes might reflect the relative abundance and physiological importance of PPa1 and PPa2 in roots (Figure 1, Table 1; Supplemental Figure 6). Cell type-specific phenotypes, such as abnormal swelling in *fugu5-1 ppa1-1* root cells above the elongation zone (Figure 6), might reflect the

abundance of PPa1 exclusively in this region (Table 1; Supplemental Figure 6). By contrast, PPa2 expression was limited to the root meristematic zone (Table 1; Supplemental Figure 6), which may explain the moderate phenotype of *fugu5-1 ppa2-1* in the root elongation zone (Figure 4), with the absence of cell swelling (Figure 6F) and a gradual increase in S4B staining intensity from the division zone to the elongation zone (Supplemental Figure 12A).

On the other hand, the leaves of *fugu5*s *ppa1-1* and *fugu5*s *ppa4-1* were atrophied (Figure 3; Supplemental Figures 10 and 11). The severe phenotype of *fugu5*s *ppa1-1* leaves points to the physiological importance of PPa1 in this organ. The leaf atrophy of *fugu5*s *ppa4-1* might be related to the extensive expression of PPa4 in young, emerging leaves (Table 1; Supplemental Figure 4). Leaf atrophy has been reported in the *fugu5-1*, *fugu5-3*, and *vhp1* single mutants grown on ammonium-free medium (Fukuda et al., 2016). In this study, we detected leaf atrophy in both *fugu5-1 ppa1-1* and *fugu5-1 ppa4-1* seedlings, even when grown on 0.5× MS medium with sufficient levels of ammonium (Figure 3; Supplemental Figure 10). Under the same conditions, *fugu5*s seedlings did not exhibit leaf atrophy. Therefore, *fugu5*s *ppa1-1* and *fugu5*s *ppa4-1* plants are more sensitive to conditions in the medium than *fugu5*s. The leaf atrophy in the mutants could be attributed to increased PPi levels, as this phenotype was recovered by the introduction of PPa1 or PPa4 (Supplemental Figure 11). Metabolomics studies of these mutants should provide important information about the biochemical mechanisms underlying leaf atrophy.

### $H^+$-PPase Is the Key Scavenging Enzyme of Cytosolic PPi

Previous and current results confirm that all five PPa isozymes have PPi hydrolysis activity. Nevertheless, the *ppa1,2,4,5* quadruple mutant showed no visible phenotype (Figures 3 to 5), whereas single knockout mutants of $H^+$-PPase genes (*fugu5s* and *vhp1-1*) exhibit clear phenotypes (Figures 3 and 5) (Ferjani et al., 2011; Asaoka et al., 2016; Fukuda et al., 2016). These results indicate that $H^+$-PPase and the other cytosolic PPases fully complemented the lack of PPa1, PPa2, PPa4, and PPa5.

The cytosol of *ppa1,2,4,5* seedlings contains at least five types of inorganic PPase: PPa3, VHP1, VHP2;1, VHP2;2, and PS2 (Segami et al., 2010; May et al., 2011). As mentioned above, the PPa3 content is negligible in vegetative tissues, except root hairs (Figure 1, Table 1; Supplemental Figures 6 and 7). PS2 is induced under phosphate-deficient conditions (May et al., 2011), and its physiological contribution may be negligible under normal conditions. The type II $H^+$-PPases, VHP2;1 and VHP2;2, are localized to the Golgi apparatus, and their levels and activities are negligible compared with VHP1 (Segami et al., 2010). Hence, the vacuolar $H^+$-PPase VHP1 might have sufficient activity to complement the lack of the four PPa isozymes.

Conversely, defects in VHP1 alone caused an increase in PPi content (Figure 5C) (Ferjani et al., 2011). The even higher levels of PPi in *fugu5-1 ppa1-1* seedlings indicate that PPa1 functions in *fugu5-1* to partially compensate for the lack of VHP1. Taken together, these findings indicate that Arabidopsis $H^+$-PPase is the principal enzyme for maintaining adequate cytosolic PPi levels, at least under normal culture conditions.

Notably, the activities of the remaining PPa isozymes in the *VHP1* knockout mutant were only partially complemented. The PPi hydrolysis activity of $H^+$-PPase is coupled with $H^+$ pumping; the reaction velocity is only moderate due to its complicated mechanism (Nakanishi et al., 2003). Mung bean (*Vigna radiata*) $H^+$-PPase has a lower $K_m$ for PPi (4.6 μM for Mg-$PPi_2$) and a higher $k_{cat}$ (14 $s^{-1}$) (Nakanishi et al., 2003) than Arabidopsis PPa1 and PPa4 when expressed in *E. coli* (93 and 101 μM for PPi; 9.20 and 9.28 $s^{-1}$, respectively) (Navarro-De la Sancha et al., 2007), indicating that $H^+$-PPase can reduce cytosolic PPi concentrations to a level lower than that achieved by PPa isozymes. Indeed, $H^+$-PPase is abundant, accounting for 10% of total tonoplast proteins in young tissues (Maeshima, 2001). Further experiments aimed at quantifying the levels and activities of PPa isozymes may provide a better understanding of their contributions.

$H^+$-PPase has dual functions, namely, catalyzing PPi hydrolysis in the cytosol and facilitating active translocation of protons into the vacuole. Thus, an adequate concentration of PPi is essential for the full activity of $H^+$-PPase and other PPi-utilizing enzymes. We speculate that plants might maintain cytosolic PPi at adequate levels through the reduction of PPa activity. Cytosolic PPa isozymes may serve as an emergency system for scavenging PPi when present in the cytosol at extremely high levels (Figure 11A).

### PPi Accumulation Causes Weakness and Morphological Changes in the Cell Wall

The *fugu5-1 ppa1-1* mutant exhibited severe phenotypes in both the shoot and root (Figures 3 and 4), as well as swollen cells with incomplete cell walls in the root elongation zone (Figures 6E, 6I, and 6J). This swelling phenotype mimics the cell wall defect observed in plants treated with isoxaben (Figure 6B) and in *prc1/cesA6* (PROCUSTE1/CELLULOSE SYNTHASE6) and *rsw1/cesA1* (RADIALLY SWELLEN1/CELLULOASE SYNTHASE1) mutants, which lack cellulose synthase (Baskin et al., 1992; Arioli et al., 1998; Fagard et al., 2000; Desprez et al., 2002). Furthermore, sucrose feeding reinforced the morphological changes in *fugu5-1 ppa1-1* roots (Figures 4B and 4C), which also resembled cell wall-deficient mutants *fei1 fei2*, *sos5*, *prc1*, and *cob*, as well as wild-type plants treated with isoxaben (Xu et al., 2008). Incomplete cell walls (referred to as stubs) have been observed in both the cellulose synthase mutant *prc1* and the callose synthase mutant *massue/gsl8* (Fagard et al., 2000; Chen et al., 2009; Thiele et al., 2009). The stubs in *prc1* form during cell elongation due to the tearing of weak cell walls. The formation of stubs in *gsl8* is due to a deficiency in callose, which is essential for cell plate formation during cell division. Young *fugu5-1 ppa1-1* cells possess stubs and lack cell plate-forming vesicles (Figures 6I and 6J), indicating they are defective in callose synthesis and cell plate formation. Consistently, Aniline Blue staining revealed poor, incomplete deposition of callose in the cell plates of *fugu5-1 ppa1-1* (Figure 8H).

Cell walls provide structural strength to plant cells and determine cell shape. Although plant cells are normally resistant to low osmotic conditions, *fugu5-1 ppa1-1* root tips burst under hyperosmotic shock (Figures 7A and 7D; Supplemental Movies 1 and 2), indicating that the cell walls in the double mutant were very weak in the face of increasing turgor pressure. This cell wall weakness

was partially mimicked by treatment with isoxaben, an inhibitor of CESA3 and CESA6 trafficking to the plasma membrane (Fisher and Cyr, 1998; Paredez et al., 2006; Tateno et al., 2016) (Figure 7B; Supplemental Movies 3 and 4). The damage was more severe in *fugu5-1 ppa1-1* than in isoxaben-treated wild-type plants, and *fugu5-1 ppa1-1* roots burst, whereas the root tips of isoxaben-treated wild-type plants did not. Indeed, we detected a notable decrease in cellulose levels in the epidermis of *fugu5-1 ppa1-1* (Figures 8A to 8D). The decrease in the non-starch Glc ratio detected in etiolated seedlings also points to reduced cellulose levels in *fugu5-1 ppa1-1* (Figure 9). By contrast, isoxaben-treated roots exhibited normal cellulose levels, at least in the epidermis (Figure 8D; Supplemental Figure 12) and therefore did not burst in response to hypotonic conditions (Figure 7B; Supplemental Movies 3 and 4).

Cell wall polysaccharides including callose, cellulose, hemicellulose, and pectin are synthesized from sugar nucleotides. Reactions leading to the biosynthesis of sugar nucleotides from sugar phosphates and nucleotides generate PPi and are mainly detected in the cytosol (Seifert, 2004). Therefore, high cytosolic PPi levels should inhibit sugar nucleotide biosynthesis, particularly in these actively growing cells. However, *fugu5-1 ppa1-1* root tips were stained normally by Ruthenium Red (Figures 8E and 8F). TEM analysis revealed that the cell walls of the epidermis and lateral root cap were quite thick (Supplemental Figures 12D and 12E). The changes in monosaccharide composition in the cell walls of etiolated seedlings also indicate that the inhibitory effect of PPi differed among polysaccharides (Figure 9). The substrates of hemicellulose side chains and pectin are transported into the Golgi

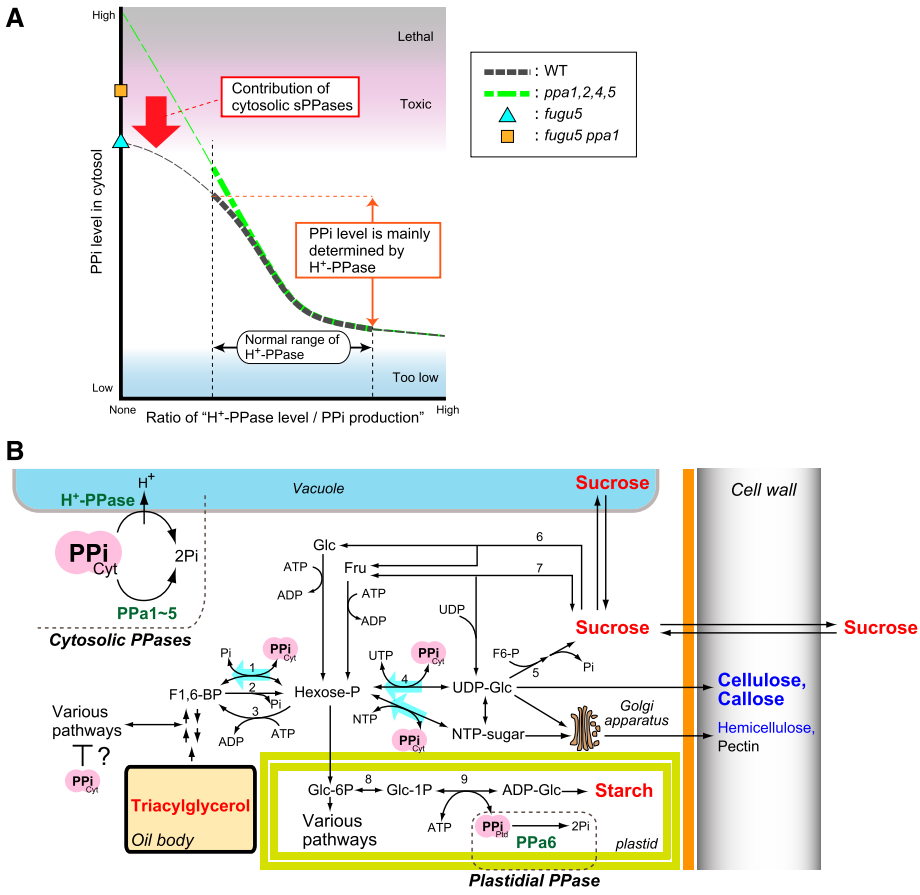


**Figure 11.** Models of the Roles of H+-PPase and sPPase in Maintaining PPi Homeostasis and Sugar Metabolism for the Biosynthesis of Sucrose and Cell Wall Components.

**(A)** Model of the physiological roles of H+-PPase and sPPase in cytosolic PPi homeostasis. The expected cytosolic PPi concentrations in the wild type, *ppa1,2,4,5*, *fugu5*, and *fugu5 ppa1* are indicated by dotted lines, a triangle (*fugu5*), and a square (*fugu5 ppa1*). H+-PPase and sPPases maintain adequate levels of PPi, as shown in the white zone. sPPases may help reduce PPi levels when H+-PPase activity is suppressed, as shown by the red arrow.
**(B)** Model of sugar metabolism in heterotrophic tissues of *fugu5-1 ppa1-1*.
Disrupting *VHP1* and *PPa1* causes a marked increase in cytosolic PPi levels, thereby biasing PPi-dependent bidirectional reactions in the PPi-degrading direction (light blue arrows). However, plastids have their own PPi environment; thus, PPi-dependent reactions including starch synthesis are not affected by increases in cytosolic PPi. Experimentally confirmed increases and decreases in the levels of components are indicated by different colors (red, increase; blue, decrease). 1, pyrophosphate-dependent phosphofructokinase; 2, fructose-1,6-bisphosphatase; 3, phosphofructokinase; 4, UGPase (UDP-Glc pyrophosphorylase); 5, sucrose phosphate synthase; 6, invertase; 7, sucrose synthase; 8, phosphoglucomutase; and 9, AGPase (ADP-Glc pyrophosphorylase).

(Seifert, 2004; Reyes and Orellana, 2008). Therefore, the biosynthesis of these cell wall components is also affected by their affinity for sugar nucleotide transporters. In addition, these substances are concentrated in the Golgi lumen, which may affect their tolerance to high cytosolic PPi concentrations.

### Starch Accumulates in Source and Sink Organs in Response to Increased PPi Levels

Ectopic starch grain formation occurred in *fugu5-1 ppa1-1* (Figure 10). The relationship between starch and PPi was previously examined by overexpressing sPPase in plants (Sonnewald, 1992; Lerchl et al., 1995; Geigenberger et al., 1998; Meyer et al., 2012; Osorio et al., 2013); however, the starch contents in transgenic plants generated in these studies varied. Theoretically, overexpressing sPPase should reduce starch biosynthesis and increase soluble sugar content due to a decrease in PPi and glucose 6-phosphate (Glc-6P) levels. Specifically, decreased cytosolic PPi levels stimulate a reaction catalyzed by UGPase: Glc-6P + UTP → UDP-Glc + PPi. Reduced Glc-6P levels suppress starch biosynthesis because Glc-6P is essential for this process in plastids (Kammerer et al., 1998). Simultaneously, sucrose is maintained at high levels.

The high starch accumulation in *fugu5-1 ppa1-1* can be explained as follows. The metabolic pathways involving sucrose, starch, triacylglycerol, pectin, and cellulose at the heterotrophic phase and in heterotrophic tissues are summarized in Figure 11B. Starch is synthesized from ADP-Glc in plastids. ADP-Glc is synthesized by AGPase: Glc-1P + ATP → ADP-Glc + PPi (Streb and Zeeman, 2012). PPi generated in plastids is hydrolyzed by plastidial PPa6 (Schulze et al., 2004). A deficiency in the genes for either plastidial phosphoglucomutase (*pgm*) or plastidial AGPase (*adg1*) results in a starchless or low-starch phenotype in Arabidopsis (Caspar et al., 1985; Lin et al., 1988; Streb et al., 2009). In contrast to plants overexpressing sPPase, the high PPi levels in the cytosol of *fugu5-1 ppa1-1* might stimulate the production of Glc-6P by UGPase. Increased Glc-6P levels stimulate starch synthesis in plastids (Figure 11B).

The sucrose concentration was markedly elevated in *fugu5-1 ppa1-1*, whereas it was reduced in *fugu5-1* (Figure 5). High sucrose levels may result from severe growth suppression. High PPi levels suppress plant growth by inhibiting macromolecule biosynthesis (Maeshima, 2001; Ferjani et al., 2011; Takahashi et al., 2017). Under these conditions, sucrose consumption might be markedly reduced in *fugu5-1 ppa1-1*. This reduced sucrose consumption may exceed the decline in sucrose supply due to the inhibition of gluconeogenesis that occurs in *fugu5* (Ferjani et al., 2011; Takahashi et al., 2017). This is a plausible scenario for why the sucrose levels were elevated in *fugu5-1 ppa1-1* plants. Sucrose feeding failed to sufficiently restore *fugu5*s *ppa1-1* growth and cellulose levels, which also supports this hypothesis (Figures 3, 5, and 8, Supplemental Figure 10). Taken together, carbohydrate metabolism is suppressed in *fugu5*s *ppa1-1*, and increased sucrose levels might stimulate metabolic flow to starch synthesis in plastids, in which PPa6 regulates PPi levels.

In conclusion, cytosolic PPa isozymes are expressed in a tissue- and growth stage-specific manner, with variable abundance. The physiological roles of PPa isozymes are masked by $H^+$-PPase, which is abundant in most plant cells. Our analysis of the severe phenotypes of *fugu5 ppa1* mutants unveiled the hidden contribution of PPa isozymes in plants. Finally, dysfunction in the cooperative regulation of PPi by $H^+$-PPase and the PPa isozymes led to a marked increase in PPi levels, which in turn triggered ectopic starch accumulation in both heterotrophic and photosynthetic tissues, as well as incomplete cell wall formation.

## METHODS

### Plant Materials

*Arabidopsis thaliana* (accession Columbia-0) seeds, which were provided by the Riken Bioresource Center, were surface-sterilized, placed in the dark at 4°C for 2 d and sown in plates on 0.5× MS medium containing 2.5 mM MES-KOH, pH 5.7, sucrose, and gellan gum (Wako Pure Chemical Industries). To avoid the buildup of excess moisture, the concentration of the gellan gum varied according to sucrose concentration: 0% sucrose with 1% gellan gum, 1% sucrose with 0.75% gellan gum, and 2% sucrose with 0.5% gellan gum.

The plates were incubated at 22°C for 2 to 3 weeks under long-day conditions (16/8-h light/dark cycle with white light fluorescent lamps at ~90 $\mu$mol $m^{-2}$ $s^{-1}$). For further analysis, the plants were transferred to soil in pots and grown in a greenhouse at 22°C under long-day conditions. The pots were irrigated twice weekly with Molecular Genetics Research Laboratory (MGRL) medium (Naito et al., 1994) supplemented with 0.5 mM $NH_4NO_3$. Prior to analysis, *ppa1-1*, *ppa2-1*, *ppa4-1*, and *ppa5-1* were backcrossed three times with the wild type. The T-DNA insertion sites were determined by DNA sequencing (Supplemental Figure 1). To complement *fugu5-1 ppa1-1* with *IPP1*, *fugu5-1 ppa1-1* was crossed with *AVP1*$_{pro}$*:IPP1* (Ferjani et al., 2011), and *IPP1*$^{+/+}$*fugu5-1*$^{-/-}$*ppa1-1*$^{-/-}$ plants were selected in the F2 generation.

### Vector Construction

The PCR primers used in this study are listed in Supplemental Table 1. To clone PPa isogenes from the Arabidopsis genome, *PPa1* (−1985 to +1707 bp), *PPa2* (−1876 to +1681 bp), *PPa3* (−2008 to +1527 bp), *PPa4* (−2047 to +2382 bp), and *PPa5* (−884bp to +1685 bp) were amplified from genomic DNA using KOD-plus DNA polymerase (Toyobo). The resulting DNA fragments were subcloned into the *Eco*RV site of the pZErO 2.1 plasmid (Thermo Fisher Scientific). To construct PPa-cfGFP, the GFP variant cfSGFP2 (Suzuki et al., 2012) was constructed by site-specific mutation of C48S, F64L, C70M, S72A, M153T, V163A, and S175G toward the [$Gly_4Ser$]×2-mGFP (M1A, A207K) of pGWB501-VHP1-mGFP (Segami et al., 2014).

To elongate the N terminus linker, an additional 5-amino acid sequence was added to cfSGFP2_set1_Fw. Three sets of DNA fragments were amplified from [$Gly_4Ser$]x2-mGFP using primers including the mutation shown above and fused by PCR to obtain [$Gly_4Ser$]x3-cfGFP.

To construct PPa1-cfGFP, PPa2-cfGFP, and PPa3-cfGFP, the coding region with its promoter and 3′UTR with the *GFP* sequence were amplified from pZErO2-PPa individually. [$Gly_4Ser$]x3-cfGFP was conjugated with 20 bp of each *PPa* genomic fragment by adding the extra sequence to the forward primer. The promoter + coding region, 3′UTR, and pZErO2.1 were digested with the following sets of restriction enzymes: *Kpn*I, *Xba*I, and *Spe*I + *Not*I for PPa1-cfGFP; *Kpn*I, *Xba*I, and *Bam*HI + *Xho*I for PPa2-cfGFP and PPa3-cfGFP. These four DNA fragments were fused using an In-fusion HD Cloning Kit (Clontech Laboratories) to obtain each pZErO2-PPa-GFP. The *PPa-GFP* fusions were excised with *Kpn*I and *Not*I and subcloned into the pENTR-2B vector (Thermo Fisher Scientific).

To construct PPa4-cfGFP and PPa5-cfGFP, vector conversion of pZErO2-PPa from pZErO2 to pENTR-2B was performed using *Kpn*I and *Not*I. The coding region, 3′UTR, and linker-cfGFP were amplified and fused

by PCR, and the PPa-GFP-3′UTR fragment was inserted into pENTR-PPa using *Hind*III or *Sca*I and *Not*I. The vector portions of the five entry vectors listed above were replaced with the pGWB501 binary vector (Nakagawa et al., 2007) using LR Clonase II (Invitrogen).

### Construction of Complementation Vectors

To complement *fugu5-1 ppa1-1*, *fugu5-1 ppa2-1*, and *fugu5-1 ppa4-1* with *PPa1*, *PPa2*, and *PPa4* genomic DNA, respectively, the DNA was excised from pZErO2-sPPases with *Kpn*I and *Not*I as described in the Methods and subcloned into the pENTR-2B vector (Thermo Fisher Scientific). The vector portions of the entry vectors were replaced with pGWB501 binary vectors using LR Clonase II (Invitrogen) to obtain pGWB501-PPa1, pGWB501-PPa2, and pGWB501-PPa4.

### Generation of Transgenic Plants

Plants were transformed with *Agrobacterium radiobacter* strain C58C1 carrying the pGWB501-based binary vectors by the floral dip method (Clough and Bent, 1998). The transformants were grown on 0.5× MS/gellan gum plates containing 7.5 $\mu$g mL$^{-1}$ hygromycin and 0.2 mg mL$^{-1}$ Cefotax (Chugai Pharmaceutical).

### Genotyping

To select sPPase knockout mutants, genomic DNA was extracted from cotyledons (Thomson and Henry, 1995). Specific primer pairs used for selection are shown in Supplemental Table 1. DNA was amplified using KOD-FX Neo (Toyobo).

To select *fugu5-1*$^{-/-}$ from a population of heterozygous plants of the *fugu5-1* genotype, genomic DNA was purified from transgenic plants and amplified using r-Taq DNA polymerase (Toyobo) with specific primers (*fugu5-1*-Fw and *fugu5-1*-Rv; Table 1). The amplified DNA was treated with *Sph*I, and *fugu5-1*$^{-/-}$ lines were selected based on the sizes of the *Sph*I products.

### Iodine Staining

Root and hypocotyl samples were fixed in 4% (w/v) paraformaldehyde in PBS for 30 to 120 min under a vacuum at room temperature. Leaf samples were fixed overnight in acetic acid: ethanol at a 1:3 ratio. The solvent was gradually replaced with PBS in an ethanol series. The fixed tissues were washed twice for 1 min in PBS and cleared with ClearSee version 1 (10% [w/v] xylitol, 15% [w/v] sodium deoxycholate, and 25% [w/v] urea) (Kurihara et al., 2015). Sodium deoxycholate has weak decolorizing activity for iodine staining, so the samples were transferred to 10% (w/v) xylitol and 25% (w/v) urea. Finally, the tissues were stained in 2 mM iodine (Wako), 10% xylitol, and 25% urea.

### Microscopy

Bright-field and epifluorescence images were obtained using an upright BX51 microscope (Olympus) and captured with a DP72 or DP73 camera (Olympus). For epifluorescence imaging, a U-MNIBA2 or U-MWIG2 filter cube equipped for GFP or PI, respectively, was used. Macro images were observed under a SZ61 stereomicroscope (Olympus) and captured with a DP50 camera (Olympus). CLSM observations were conducted with an upright FV1000-D CLSM (Olympus). The excitation wavelength and transmission range for emission were 473/485 to 560 nm for GFP, 473/650 to 750 nm for chlorophyll, 473/617 to 717 nm for PI, 559/570 to 670 nm for S4B, and 405/425 to 525 nm for Aniline Blue. The images were obtained using Olympus FluoView software and a UPLSAPO60XW water immersion objective or a UPLSAPO 10× objective lens (Olympus). To quantify S4B intensity, the free line region of interest was set between the lateral root cap and the epidermis excluding crushed cells, and the intensity value was recorded. The intensity values were quantified and 3D images of the cell plate were constructed using FluoView software (Olympus).

### Expression of GAL1-Driven *IPP1* in Yeast

An inducible/repressive *IPP1* gene in yeast driven by a *GAL1* promoter was constructed as previously reported (Drake et al., 2010). The *His3* and *GAL1* promoters were amplified from pRS413 (Brachmann et al., 1998) and pYES2 (Thermo Fisher Scientific), respectively. The genomic sequences of the *IPP1* upstream region and the *IPP1* CDS were amplified from yeast genomic DNA prepared from BY4741 yeast cells (Brachmann et al., 1998). The four DNA fragments were connected by PCR using their complementary sequences with amplifying primers to obtain *IPP1*upstream-*His3*-*GAL1*pro-*IPP1*. After subcloning into pBluescript-KS(−) and checking the sequences, the DNA was excised with *Sal*I and *Sac*I and transformed into BY4741. The homologous recombinant yTT1, in which the endogenous *IPP1* promoter was replaced with the *GAL1* promoter, was selected on medium containing galactose without histidine or uracil (−histidine, −uracil, and +galactose media).

### Yeast Transformation

The *IPP1* promoter (1171 bp) and *IPP1* terminator (370 bp) were amplified from yeast DNA and subcloned into pRS416 using *Sac*I and *Xba*I, and *Xho*I and *Kpn*I, respectively, to obtain *pRS-IPP1*$_{pro}$. The CDS of *PPa1-5* and *IPP1* were amplified by PCR from Arabidopsis cDNA or yeast genomic DNA and cloned into pRS-IPP1$_{pro}$ using the restriction enzyme pair *Eco*RI and *Sal*I for *PPa1* and *IPP1*; *Eco*RI and *Xho*I for *PPa2*, *PPa3*, and *PPa5*; and *Eco*RI and *Hind*III for *PPa4*. After checking the sequences, the *pRS-IPP1*$_{pro}$*:sPPases* were introduced into yTT1 competent cells by lithium acetate/single-stranded DNA/polyethylene glycol transformation (Gietz and Schiestl, 2007).

### SDS-PAGE and Immunoblotting

Crude membrane and soluble fractions were prepared from Arabidopsis plants as described previously (Segami et al., 2014). After centrifugation at 100,000*g* for 10 min at 4°C, the supernatant was used as the soluble fraction and the pellet was resuspended in a solution of 20 mM Tris-acetate, pH 7.5, 0.25 M sorbitol, 1 mM EGTA-Tris, 1 mM $MgCl_2$, and 2 mM DTT and used as the crude membrane fraction.

Proteins were separated by SDS-PAGE and transferred to an Immobilon-P membrane (EMD Millipore). After treatment with 1% ECL blocking reagent (GE Healthcare) or 3% skim milk, the membrane filter was incubated with primary antibody (1:4000 dilution), followed by horseradish peroxidase-conjugated goat anti-rabbit IgG (1:5000 dilution) (catalog no. 65-6120, lot QE215051; Thermo Fisher Scientific). H+-PPase was detected using a previously prepared antibody against the substrate binding motif of H+-PPase (Segami et al., 2010). To detect PPa isozymes, peptide-specific antibodies were prepared against the common region of Arabidopsis PPa1-PPa5 (C+MPMIDQGEKDDKII) and used as anti-PPa antibodies. Commercially available anti-GFP (catalog no. ab290; lot GR3184825-1; Abcam) and anti-IPP1 (catalog no. AP21326BT-N; lot 6002; Acris Antibodies) antibodies were used for detection of GFP and IPP1, respectively. The chemiluminescence reagent ECL or ECL-prime (GE Healthcare) was used for antigen detection. Chemiluminescence was detected with a Light-Capture II imaging device with a cooled CCD camera (Atto).

### 2D-PAGE

For isoelectric-focusing, samples were frozen in liquid nitrogen and homogenized with a mortar and pestle. After the addition of chilled acetone (1 mL) containing 10% trichloroacetate and 20 mM DTT, the homogenate was chilled at −20°C for 1 h. After centrifugation for 10 min, the precipitate was washed twice with acetone containing 20 mM DTT and incubated at

−20°C for 1 h. The precipitate was dried in an evaporator for 20 min and melted in a 50-fold volume of 7 M urea, 2 M thiourea, 3% CHAPS, 1% Triton X-100, and 20 mM DTT. The sample was subjected to ultracentrifugation at 40,000 rpm and 4°C for 8 min in an SA45 rotor (Hitachi). After adding a one-tenth volume of 1 M Tris-HCl, pH 9.5, and 1 M acrylamide, the supernatant was subjected to A-M58 IEF agarGEL (pH range 5−8; Atto) electrophoresis at a constant voltage of 360 V for 160 min. After separation, the gel was fixed in 10% trichloroacetic acid for 3 min, washed three times with distilled water, and incubated in distilled water for 120 min. The gel was equilibrated with 50 mM Tris-HCl, pH 6.8, 2% SDS, and 0.001% bromophenol blue for 10 min with gentle agitation, followed by SDS-PAGE.

### Quantification of PPi and Sucrose

Approximately 200 to 300 etiolated seedlings at 3.5 DAS were homogenized in 0.2× volume of 3 M $HClO_4$ on ice with a BioMasher II (Nippi). The homogenate was incubated on ice for 15 min to precipitate proteins and centrifuged at 20,000*g* for 10 min at 4°C. The supernatant was transferred to a fresh tube, along with 25 mg of the metal scavenger SiliaMetS TAAcOH (SiliCycle) and gradually neutralized with KOH. The sample was centrifuged at 20,000*g* for 10 min at 4°C to remove $KClO_4$ and SiliaMetS. The supernatant was passed twice through a Monospin C18 column (GL Sciences). The flow-through fraction was diluted with water and filtered through a MILLEX-GV 0.22-μm filter (Millipore). PPi and sucrose levels were measured by ion chromatography with a DX-500 system (Dionex) using an IonPac AS11 column (Dionex) for PPi and a CarboPac PA1 column (Dionex) for sucrose.

### Quantification of Total TAG

Total TAG levels were quantified as described previously, with minor modifications (Ferjani et al., 2011). Either 20 dry seeds or 20 etiolated seedlings at 3 DAS were homogenized in a mortar or BioMasher II homogenizer (Nippi) with 50 μL distilled water. The homogenates were combined with 0.5 mL triglyceride E-Test (Wako) and incubated at 37°C for 5 min. The supernatants (200 μL) were transferred to 96-well plates, and absorbance at 600 nm was quantified with an Enspire 2300 plate reader (Perkin-Elmer).

### Cell Wall Staining

Arabidopsis plants were grown on MS plates containing 1% sucrose for 5 to 8 d, and the roots were fixed overnight in FAA (50% ethanol, 5% acetic acid, and 4% formaldehyde) at room temperature. The samples were gradually rehydrated through an ethanol series, washed with PBS, and cleared with ClearSee (Kurihara et al., 2015). For S4B staining, samples were stained with 0.01% S4B in xylitol/urea/NaCl (10% xylitol, 25% urea, and 150 mM NaCl) for 30 min, washed with xylitol/urea/NaCl, and observed via CLSM. For Aniline Blue staining, the rehydrated samples were stained with 0.05% decolorized Aniline Blue, 54 mM $K_3PO_4$ (pH 11), 10% xylitol, and 25% urea for 1 h and observed by CLSM. Aniline Blue decolorization was performed according to Mori et al. (2006). For Ruthenium Red staining, samples fixed in FAA were dehydrated through an ethanol series, embedded in Technovit 7100 (Kulzer and Co.) following the manufacturer's protocol, and sectioned with a microtome (RM2125 RTS; Leica Microsystems) to a thickness of 5 μm as described previously (Maeda et al., 2014). The histological sections were stained with 0.02% Ruthenium Red for 30 min, washed with water for 30 s, and examined using a light microscope (DM6 B; Leica Microsystems).

### Sugar Composition Analysis

AIR and monosaccharide composition analyses were performed as described previously (Sakamoto and Mitsuda, 2015; Sakamoto et al., 2015). Starch content was determined using the modified protocol of the Resistant Starch Assay Kit (Megazyme). Starch in powdered AIR (2.00–3.00 mg) was digested with 500 units $mL^{-1}$ α-amylase from porcine pancreas (Megazyme) and 0.33 units $mL^{-1}$ amyloglucosidase from *Aspergillus niger* (Megazyme) at 37°C for 18 h. Liberated glucose, reflecting starch levels, was measured using a Glucose C II Test Kit (Wako).

### Statistical Analysis

To quantify fresh weight, length, thickness, and concentration, data from at least three independent experiments were averaged, and the values were subjected to statistical analyses using Student's *t* test, or Tukey's honestly significant difference (HSD) test (R version 3.1.2; R Core Team, 2014). For ratio quantification, the values were subjected to statistical analysis using the prop test (R version 3.1.2; R Core Team, 2014).

### Accession Numbers

Sequence data from this article can be found in the GenBank/EMBL/DDBJ libraries under the following accession numbers: Arabidopsis *VHP1* (AT1G15690.1), *PPa1* (AT1G01050.1), *PPa2* (AT2G18230.1), *PPa3* (AT2G46860.1), *PPa4* (AT3G53620.1), *PPa5* (AT4G01480.1), *PPa6* (AT5G09650.1), *VHP2;1* (AT1G78920), *VHP2;2* (AT1G16780), and *PS2*/*PPSPASE1* (AT1G73010).

### Supplemental Data

**Supplemental Figure 1.** Identification of T-DNA insertional mutants.

**Supplemental Figure 2.** Immunological detection of PPase isozymes.

**Supplemental Figure 3.** GFP-fused pyrophosphatases complement the double mutant phenotypes.

**Supplemental Figure 4.** Tissue-specific accumulation of PPa-GFP in seedlings.

**Supplemental Figure 5.** Intracellular localization of PPa-GFP in leaves.

**Supplemental Figure 6.** Cell-specific and intracellular localization of PPa-GFP in roots.

**Supplemental Figure 7.** Epifluorescent microscopy images of 2-DAG etiolated seedlings expressing PPa1, PPa2, PPa4, PPa3, PPa5, and VHP1 fused with GFP.

**Supplemental Figure 8.** Distribution of PPa isozymes in flowers.

**Supplemental Figure 9.** Complementation of IPP1-defective yeast strain yTT1 by Arabidopsis PPa.

**Supplemental Figure 10.** Growth phenotypes of double mutants of *fugu5-3* with *ppa1-1*, *ppa2-1*, *ppa4-1*, and *ppa5-1*.

**Supplemental Figure 11.** Complementation of *fugu5-1 ppa1-1*, *fugu5-1 ppa2-1*, and *fugu5-1 ppa4-1* by *PPa1*, *PPa2*, and *PPa4*.

**Supplemental Figure 12.** Complementary data for Figure 8.

**Supplemental Table 1.** List of oligonucleotide primers used in this study.

**Supplemental Movie 1.** Time-lapse imaging of a water-submerged *fugu5-1 ppa1-1* root tip.

**Supplemental Movie 2.** Time-lapse imaging of PI staining.

**Supplemental Movie 3.** Time-lapse imaging of a water-submerged wild-type root tip treated with 5 nM isoxaben for 3 d.

**Supplemental Movie 4.** Time-lapse imaging of PI staining.

**Supplemental Movie Legends.**

## ACKNOWLEDGMENTS

We thank Yoichi Nakanishi and Miki Kawachi (Nagoya University, Japan) for their valuable advice. This work was supported by JSPS KAKENHI Grants 26252011 and 26113506 to M.M. and 2816K18687 to S. Segami and by a Grant-in-Aid for Scientific Research (B) (16H04803 to A.F.).

## AUTHOR CONTRIBUTIONS

S. Segami and M.M. designed the experiments and wrote and finalized the manuscript. S. Segami established the knockout mutant lines and conducted the phenotyping and construction of PPa4-cfGFP and PPa5-cfGFP, microscopy observations, quantification of PPi and sucrose, and biochemical and physiological analyses. T.T. constructed PPa1-cfGFP, PPa2-cfGFP, and PPa3-cfGFP and performed the yeast experiments and IPP1 complementation assays. M.F. performed the physiological analyses. S. Segami and S.G. performed sectioning and cell wall staining. S. Sakamoto and N.M. performed the sugar composition analysis. S.K. improved the iodine staining method. A.F. provided the *fugu5s* mutants and *AVP1*$_{pro}$*:IPP1* transgenic lines and finalized the manuscript.

Received December 1, 2017; revised April 5, 2018; accepted April 23, 2018; published April 24, 2018.

## REFERENCES

**Anderson, C.T., Carroll, A., Akhmetova, L., and Somerville, C.** (2010). Real-time imaging of cellulose reorientation during cell wall expansion in Arabidopsis roots. Plant Physiol. **152:** 787–796.

**Arioli, T., et al.** (1998). Molecular analysis of cellulose biosynthesis in *Arabidopsis.* Science **279:** 717–720.

**Asaoka, M.M., Segami, S., Ferjani, A., and Maeshima, M.** (2016). Contribution of PPi-hydrolyzing function of vacuolar H+-pyrophosphatase in vegetative growth of *Arabidopsis*: evidenced by expression of uncoupling mutated enzymes. Front. Plant Sci. **7:** 415.

**Bailey, J.M., and Whelan, W.J.** (1961). Physical properties of starch. I. Relationship between iodine stain and chain length. J. Biol. Chem. **236:** 969–973.

**Baskin, T.I., Betzner, A.S., Hoggart, R., Cork, A., and Williamson, R.E.** (1992). Root morphology mutants in *Arabidopsis thaliana.* Aust. J. Plant Physiol. **19:** 427–437.

**Brachmann, C.B., Davies, A., Cost, G.J., Caputo, E., Li, J., Hieter, P., and Boeke, J.D.** (1998). Designer deletion strains derived from *Saccharomyces cerevisiae* S288C: a useful set of strains and plasmids for PCR-mediated gene disruption and other applications. Yeast **14:** 115–132.

**Caspar, T., Huber, S.C., and Somerville, C.** (1985). Alterations in growth, photosynthesis, and respiration in a starchless mutant of *Arabidopsis thaliana* (L.) deficient in chloroplast phosphoglucomutase activity. Plant Physiol. **79:** 11–17.

**Chen, J., Brevet, A., Fromant, M., Lévêque, F., Schmitter, J.M., Blanquet, S., and Plateau, P.** (1990). Pyrophosphatase is essential for growth of *Escherichia coli.* J. Bacteriol. **172:** 5686–5689.

**Chen, X.-Y., Liu, L., Lee, E., Han, X., Rim, Y., Chu, H., Kim, S.-W., Sack, F., and Kim, J.-Y.** (2009). The Arabidopsis callose synthase gene GSL8 is required for cytokinesis and cell patterning. Plant Physiol. **150:** 105–113.

**Clough, S.J., and Bent, A.F.** (1998). Floral dip: a simplified method for *Agrobacterium*-mediated transformation of *Arabidopsis thaliana.* Plant J. **16:** 735–743.

**de Graaf, B.H.J., Rudd, J.J., Wheeler, M.J., Perry, R.M., Bell, E.M., Osman, K., Franklin, F.C.H., and Franklin-Tong, V.E.** (2006). Self-incompatibility in Papaver targets soluble inorganic pyrophosphatases in pollen. Nature **444:** 490–493.

**Desprez, T., Vernhettes, S., Fagard, M., Refrégier, G., Desnos, T., Aletti, E., Py, N., Pelletier, S., and Höfte, H.** (2002). Resistance against herbicide isoxaben and cellulose deficiency caused by distinct mutations in same cellulose synthase isoform CESA6. Plant Physiol. **128:** 482–490.

**Drake, R., Serrano, A., and Pérez-Castiñeira, J.R.** (2010). N-terminal chimaeras with signal sequences enhance the functional expression and alter the subcellular localization of heterologous membrane-bound inorganic pyrophosphatases in yeast. Biochem. J. **426:** 147–157.

**Eaves, D.J., Haque, T., Tudor, R.L., Barron, Y., Zampronio, C.G., Cotton, N.P.J., de Graaf, B.H.J., White, S.A., Cooper, H.J., Franklin, F.C.H., Harper, J.F., and Franklin-Tong, V.E.** (2017). Identification of phosphorylation sites altering pollen soluble inorganic pyrophosphatase activity. Plant Physiol. **173:** 1606–1616.

**Fagard, M., Desnos, T., Desprez, T., Goubet, F., Refregier, G., Mouille, G., McCann, M., Rayon, C., Vernhettes, S., and Höfte, H.** (2000). *PROCUSTE1* encodes a cellulose synthase required for normal cell elongation specifically in roots and dark-grown hypocotyls of *Arabidopsis.* Plant Cell **12:** 2409–2424.

**Ferjani, A., Horiguchi, G., Yano, S., and Tsukaya, H.** (2007). Analysis of leaf development in *fugu* mutants of *Arabidopsis* reveals three compensation modes that modulate cell expansion in determinate organs. Plant Physiol. **144:** 988–999.

**Ferjani, A., Segami, S., Horiguchi, G., Muto, Y., Maeshima, M., and Tsukaya, H.** (2011). Keep an eye on PPi: the vacuolar-type H+-pyrophosphatase regulates postgerminative development in Arabidopsis. Plant Cell **23:** 2895–2908.

**Ferjani, A., Segami, S., Asaoka, M., and Maeshima, M.** (2014). Regulation of PPi levels through the vacuolar membrane H+-pyrophosphatase. In Progress in Botany 75, U. Lüttge, W. Beyschlag, and J. Cushman, eds (Berlin, Heidelberg: Springer-Verlag), pp. 145–165.

**Fisher, D.D., and Cyr, R.J.** (1998). Extending the microtubule/microfibril paradigm. Cellulose synthesis is required for normal cortical microtubule alignment in elongating cells. Plant Physiol. **116:** 1043–1051.

**Fukuda, M., Segami, S., Tomoyama, T., Asaoka, M., Nakanishi, Y., Gunji, S., Ferjani, A., and Maeshima, M.** (2016). Lack of H+-pyrophosphatase prompts developmental damage in *Arabidopsis* leaves on ammonia-free culture medium. Front. Plant Sci. **7:** 819.

**Geigenberger, P., Hajirezaei, M., Geiger, M., Deiting, U., Sonnewald, U., and Stitt, M.** (1998). Overexpression of pyrophosphatase leads to increased sucrose degradation and starch synthesis, increased activities of enzymes for sucrose-starch interconversions, and increased levels of nucleotides in growing potato tubers. Planta **205:** 428–437.

**George, G.M., van der Merwe, M.J., Nunes-Nesi, A., Bauer, R., Fernie, A.R., Kossmann, J., and Lloyd, J.R.** (2010). Virus-induced gene silencing of plastidial soluble inorganic pyrophosphatase impairs essential leaf anabolic pathways and reduces drought stress tolerance in *Nicotiana benthamiana*. Plant Physiol. **154:** 55–66.

**Gietz, R.D., and Schiestl, R.H.** (2007). High-efficiency yeast transformation using the LiAc/SS carrier DNA/PEG method. Nat. Protoc. **2:** 31–34.

**Gómez-García, M.R., Losada, M., and Serrano, A.** (2006). A novel subfamily of monomeric inorganic pyrophosphatases in photosynthetic eukaryotes. Biochem. J. **395:** 211–221.

**Gutiérrez-Luna, F.M., Navarro de la Sancha, E., Valencia-Turcotte, L.G., Vázquez-Santana, S., and Rodríguez-Sotres, R.** (2016).

Evidence for a non-overlapping subcellular localization of the family I isoforms of soluble inorganic pyrophosphatase in *Arabidopsis thaliana.* Plant Sci. **253:** 229–242.

**Heinonen, J.K.** (2001). Biological Role of Inorganic Pyrophosphate. (Boston: Springer).

**Kammerer, B., Fischer, K., Hilpert, B., Schubert, S., Gutensohn, M., Weber, A., and Flügge, U.-I.** (1998). Molecular characterization of a carbon transporter in plastids from heterotrophic tissues: the glucose 6-phosphate/phosphate antiporter. Plant Cell **10:** 105–117.

**Koroleva, O.A., Tomlinson, M.L., Leader, D., Shaw, P., and Doonan, J.H.** (2005). High-throughput protein localization in *Arabidopsis* using *Agrobacterium*-mediated transient expression of GFP-ORF fusions. Plant J. **41:** 162–174.

**Kurihara, D., Mizuta, Y., Sato, Y., and Higashiyama, T.** (2015). ClearSee: a rapid optical clearing reagent for whole-plant fluorescence imaging. Development **142:** 4168–4179.

**Lerchl, J., Geigenberger, P., Stitt, M., and Sonnewald, U.** (1995). Impaired photoassimilate partitioning caused by phloem-specific removal of pyrophosphate can be complemented by a phloem-specific cytosolic yeast-derived invertase in transgenic plants. Plant Cell **7:** 259–270.

**Lin, T.P., Caspar, T., Somerville, C., and Preiss, J.** (1988). Isolation and characterization of a starchless mutant of *Arabidopsis thaliana* (L.) Heynh lacking ADP-glucose pyrophosphorylase activity. Plant Physiol. **86:** 1131–1135.

**Maeda, S., Gunji, S., Hanai, K., Hirano, T., Kazama, Y., Ohbayashi, I., Abe, T., Sawa, S., Tsukaya, H., and Ferjani, A.** (2014). The conflict between cell proliferation and expansion primarily affects stem organogenesis in *Arabidopsis.* Plant Cell Physiol. **55:** 1994–2007.

**Maeshima, M.** (2001). Tonoplast transporters: Organization and function. Annu. Rev. Plant Physiol. Plant Mol. Biol. **52:** 469–497.

**May, A., Berger, S., Hertel, T., and Köck, M.** (2011). The *Arabidopsis thaliana* phosphate starvation responsive gene *AtPPsPase1* encodes a novel type of inorganic pyrophosphatase. Biochim. Biophys. Acta **1810:** 178–185.

**Meyer, K., Stecca, K.L., Ewell-Hicks, K., Allen, S.M., and Everard, J.D.** (2012). Oil and protein accumulation in developing seeds is influenced by the expression of a cytosolic pyrophosphatase in *Arabidopsis.* Plant Physiol. **159:** 1221–1234.

**Mori, T., Kuroiwa, H., Higashiyama, T., and Kuroiwa, T.** (2006). GENERATIVE CELL SPECIFIC 1 is essential for angiosperm fertilization. Nat. Cell Biol. **8:** 64–71.

**Naito, S., Hirai, M.Y., Chino, M., and Komeda, Y.** (1994). Expression of a soybean (*Glycine max* [L.] Merr.) seed storage protein gene in transgenic *Arabidopsis thaliana* and its response to nutritional stress and to abscisic acid mutations. Plant Physiol. **104:** 497–503.

**Nakagawa, T., et al.** (2007). Improved Gateway binary vectors: high-performance vectors for creation of fusion constructs in transgenic analysis of plants. Biosci. Biotechnol. Biochem. **71:** 2095–2100.

**Nakanishi, Y., Yabe, I., and Maeshima, M.** (2003). Patch clamp analysis of a $H^+$ pump heterologously expressed in giant yeast vacuoles. J. Biochem. **134:** 615–623.

**Navarro-De la Sancha, E., Coello-Coutiño, M.P., Valencia-Turcotte, L.G., Hernández-Domínguez, E.E., Trejo-Yepes, G., and Rodríguez-Sotres, R.** (2007). Characterization of two soluble inorganic pyrophosphatases from *Arabidopsis thaliana.* Plant Sci. **172:** 796–807.

**Osorio, S., Nunes-Nesi, A., Stratmann, M., and Fernie, A.R.** (2013). Pyrophosphate levels strongly influence ascorbate and starch content in tomato fruit. Front. Plant Sci. **4:** 308.

**Öztürk, Z.N., Greiner, S., and Rausch, T.** (2014). Subcellular localization and developmental regulation of cytosolic, soluble pyrophosphatase isoforms in *Arabidopsis thaliana.* Turk. J. Bot. **38:** 1036–1049.

**Paredez, A.R., Somerville, C., and Ehrhardt, D.** (2006). Visualization of cellulose synthase with microtubules. Science **312:** 1491–1495.

**R Core Team** (2014). R: A Language and Environment for Statistical Computing. (Vienna, Austria: R Foundation for Statistical Computing).

**Reyes, F., and Orellana, A.** (2008). Golgi transporters: opening the gate to cell wall polysaccharide biosynthesis. Curr. Opin. Plant Biol. **11:** 244–251.

**Rojas-Beltrán, J.A., Dubois, F., Mortiaux, F., Portetelle, D., Gebhardt, C., Sangwan, R.S., and du Jardin, P.** (1999). Identification of cytosolic $Mg^{2+}$-dependent soluble inorganic pyrophosphatases in potato and phylogenetic analysis. Plant Mol. Biol. **39:** 449–461.

**Sakamoto, S., and Mitsuda, N.** (2015). Reconstitution of a secondary cell wall in a secondary cell wall-deficient *Arabidopsis* mutant. Plant Cell Physiol. **56:** 299–310.

**Sakamoto, S., Yoshida, K., Sugihara, S., and Mitsuda, N.** (2015). Development of a new high-throughput method to determine the composition of ten monosaccharides including 4-*O*-methyl glucuronic acid from plant cell walls using ultra-performance liquid chromatography. Plant Biotechnol. **32:** 55–63.

**Schulze, S., Mant, A., Kossmann, J., and Lloyd, J.R.** (2004). Identification of an *Arabidopsis* inorganic pyrophosphatase capable of being imported into chloroplasts. FEBS Lett. **565:** 101–105.

**Segami, S., Nakanishi, Y., Sato, M.H., and Maeshima, M.** (2010). Quantification, organ-specific accumulation and intracellular localization of type II H(+)-pyrophosphatase in *Arabidopsis thaliana*. Plant Cell Physiol. **51:** 1350–1360.

**Segami, S., Makino, S., Miyake, A., Asaoka, M., and Maeshima, M.** (2014). Dynamics of vacuoles and $H^+$-pyrophosphatase visualized by monomeric green fluorescent protein in *Arabidopsis*: artifactual bulbs and native intravacuolar spherical structures. Plant Cell **26:** 3416–3434.

**Seifert, G.J.** (2004). Nucleotide sugar interconversions and cell wall biosynthesis: how to bring the inside to the outside. Curr. Opin. Plant Biol. **7:** 277–284.

**Serrano-Bueno, G., Hernández, A., López-Lluch, G., Pérez-Castiñeira, J.R., Navas, P., and Serrano, A.** (2013). Inorganic pyrophosphatase defects lead to cell cycle arrest and autophagic cell death through $NAD^+$ depletion in fermenting yeast. J. Biol. Chem. **288:** 13082–13092.

**Shintani, T., Uchiumi, T., Yonezawa, T., Salminen, A., Baykov, A.A., Lahti, R., and Hachimori, A.** (1998). Cloning and expression of a unique inorganic pyrophosphatase from *Bacillus subtilis*: evidence for a new family of enzymes. FEBS Lett. **439:** 263–266.

**Sonnewald, U.** (1992). Expression of *E. coli* inorganic pyrophosphatase in transgenic plants alters photoassimilate partitioning. Plant J. **2:** 571–581.

**Sterling, C.** (1970). Crystal-structure of ruthenium red and stereochemistry of its pectic stain. Am. J. Bot. **57:** 172–175.

**Streb, S., and Zeeman, S.C.** (2012). Starch metabolism in *Arabidopsis*. The Arabidopsis Book **10:** e0160, doi/10.1199/tab.0160.

**Streb, S., Egli, B., Eicke, S., and Zeeman, S.C.** (2009). The debate on the pathway of starch synthesis: a closer look at low-starch mutants lacking plastidial phosphoglucomutase supports the chloroplast-localized pathway. Plant Physiol. **151:** 1769–1772.

**Suzuki, T., Arai, S., Takeuchi, M., Sakurai, C., Ebana, H., Higashi, T., Hashimoto, H., Hatsuzawa, K., and Wada, I.** (2012). Development of cysteine-free fluorescent proteins for the oxidative environment. PLoS One **7:** e37551.

**Takahashi, K., Morimoto, R., Tabeta, H., Asaoka, M., Ishida, M., Maeshima, M., Tsukaya, H., and Ferjani, A.** (2017). Compensated cell enlargement in *fugu5* is specifically triggered by lowered sucrose production from seed storage lipids. Plant Cell Physiol. **58:** 668–678.

**Tateno, M., Brabham, C., and DeBolt, S.** (2016). Cellulose biosynthesis inhibitors - a multifunctional toolbox. J. Exp. Bot. **67:** 533–542.

**Thiele, K., Wanner, G., Kindzierski, V., Jürgens, G., Mayer, U., Pachl, F., and Assaad, F.F.** (2009). The timely deposition of callose is essential for cytokinesis in *Arabidopsis.* Plant J. **58:** 13–26.

**Thomson, D., and Henry, R.** (1995). Single-step protocol for preparation of plant tissue for analysis by PCR. Biotechniques **19:** 394–397, 400.

**Veljanovski, V., Vanderbeld, B., Knowles, V.L., Snedden, W.A., and Plaxton, W.C.** (2006). Biochemical and molecular characterization of AtPAP26, a vacuolar purple acid phosphatase up-regulated in phosphate-deprived *Arabidopsis* suspension cells and seedlings. Plant Physiol. **142:** 1282–1293.

**Weiner, H., Stitt, M., and Heldt, H.W.** (1987). Subcellular compartmentation of pyrophosphate and alkaline pyrophosphatase in leaves. Biochim. Biophys. Acta **893:** 13–21.

**Xu, S.L., Rahman, A., Baskin, T.I., and Kieber, J.J.** (2008). Two leucine-rich repeat receptor kinases mediate signaling, linking cell wall biosynthesis and ACC synthase in *Arabidopsis.* Plant Cell **20:** 3065–3079.

**Young, T.W., Kuhn, N.J., Wadeson, A., Ward, S., Burges, D., and Cooke, G.D.** (1998). *Bacillus subtilis* ORF *yybQ* encodes a manganese-dependent inorganic pyrophosphatase with distinctive properties: the first of a new class of soluble pyrophosphatase? Microbiology **144:** 2563–2571.